

The Highly Self-Absorbed Blazar, PKS 1351–018

BRIAN PUNSLEY,^{1,2,3} SÁNDOR FREY,^{4,5} CORMAC REYNOLDS,⁶ PAOLA MARZIANI,⁷
ALEXANDER PUSHKAREV,^{8,9} SINA CHEN,¹⁰ SHANG LI,¹¹ AND PREETI KHARB¹²

¹*1415 Granvia Altamira, Palos Verdes Estates CA, USA 90274*

²*ICRANet, Piazza della Repubblica 10 Pescara 65100, Italy*

³*ICRA, Physics Department, University La Sapienza, Roma, Italy*

⁴*Konkoly Observatory, ELKH Research Centre for Astronomy and Earth Sciences, Konkoly Thege Miklós út 15-17, 1121 Budapest, Hungary*

⁵*Institute of Physics, ELTE Eötvös Loránd University, Pázmány Péter sétány 1/A, 1117 Budapest, Hungary*

⁶*CSIRO Astronomy and Space Science, PO Box 1130, Bentley WA 6102, Australia*

⁷*INAF, Osservatorio Astronomico di Padova, Italia*

⁸*Crimean Astrophysical Observatory, Nauchny 298409, Crimea, Russia*

⁹*Astro Space Center of Lebedev Physical Institute, Profsoyuznaya 84/32, Moscow 117997, Russia*

¹⁰*Physics Department, Technion Haifa, 32000, Israel*

¹¹*School of Physics and Materials Science, Anhui University, Hefei 230601, China*

¹²*National Centre for Radio Astrophysics, Tata Institute of Fundamental Research, Post Bag 3, Ganeshkhind, Pune 411007, India*

(Received ...; Revised ...; Accepted ...)

Submitted to ApJ

ABSTRACT

PKS 1351–018 at a redshift of $z = 3.71$ is one of the most luminous, steady synchrotron sources with a luminosity $> 10^{47}$ erg s⁻¹. The synchrotron luminosity does not seem to vary by more than $\sim 25\%$ over 35 years. In order to appreciate this remarkable behavior, if it were at $z = 0.5$, it would have a flux density at 15 GHz in a range of 110 – 137 Jy over 11 yrs. In spite of this steady behavior, two strong γ -ray flares $\lesssim 10^{49}$ erg s⁻¹ were detected in 2011 and 2016. There is blazar-like behavior coexisting with the steady behavior. This study is aimed at elucidating the dual nature of this source. We find that the radio source is extremely compact with a bright core and a steep spectrum secondary component, 12 mas away, that appears to be constant in position and flux density in six epochs from 1995 to 2018. We estimate that a jet with a time averaged power of $(5.2 \pm 3.2) \times 10^{45}$ erg s⁻¹ terminates in this lobe that is advancing $\gtrsim 0.9c$ at a deprojected distance of 1 – 3 kpc from the central engine. This is the rare case of a young (~ 6000 yr), very powerful radio source that is viewed a few degrees from the jet axis. We find evidence of a high velocity (4000 km s⁻¹), high

ionization wind emanating from a luminous quasar. The young radio jet appears to experience modest bending as it navigates through the intense quasar environment.

Keywords: black hole physics — galaxies: jets — galaxies: active — accretion, accretion disks

1. INTRODUCTION

The quasar PKS 1351–018 was identified as one of the most luminous of the known “ultra-luminous radio cores” with a synchrotron luminosity of $> 10^{47}$ erg s $^{-1}$ (Punsly 1995). This is a high redshift quasar at $z = 3.71$ (Osmer et al. 1994). The flux density decreases sharply at frequencies below 6.5 GHz in the quasar rest frame (Spoelstra et al. 1985). Thus, at one time, it was considered a candidate Gigahertz Peaked Spectrum (GPS) radio source with an observed spectral peak near 1.4 GHz (Spoelstra et al. 1985; O’Dea 1991). In spite of the spectral turnover below 6.5 GHz, it was later rejected as a GPS quasar due to the broad spectral peak (de Vries et al. 1997). PKS 1351–018 also has a steady spectrum based on the twenty-one 5.0 GHz (23.5 GHz in the quasar rest frame) flux density measurements from the Australia Telescope Compact Array (ATCA) calibrator web-page¹ over a 15-yr period. The mean flux density is 930 mJy with a standard deviation of 43 mJy. The measured data variation of $\pm 4.7\%$ is similar to the 5% uncertainty that is estimated for individual ATCA flux density measurements (Murphy et al. 2010). Similarly, but statistically less significant, there are eight 22.4 GHz (106 GHz in the quasar rest frame) ATCA calibrator observations over 11 yr with a mean of 543 mJy and a standard deviation of 35 mJy or 6.5%. In spite of this steady behavior, PKS 1351–018 was detected in γ -rays by the Large Area Telescope (LAT) on board the *Fermi* satellite (Ackermann et al. 2017; Li et al. 2018; Sahakyan et al. 2020). It is this dichotomy, a steady behavior near the spectral peak at cm wavelengths and the extreme blazar-like strong gamma-ray flares and enormous synchrotron luminosity, that has motivated the following detailed study of this extremely powerful jet source in the early Universe.

The paper begins with an in-depth study of the radio light curves to look for evidence of blazar-like phenomenon in Section 2. In Section 3, we consider radio interferometer imaging in order to look for blazar-like structure changes and to define the source size. In Section 4, we construct the synchrotron spectral energy distribution (SED). We analyze the optical spectrum and use it to define the energetics of the accretion flow in Section 5. We follow this up with a depiction of the γ -ray flares (Section 6). In Sections 7 and 8 we develop simple models of the stationary secondary component at ~ 12.5 mas from the nucleus. We are then able to bound the jet power. Throughout this paper, we adopt the following cosmological parameters: $H_0 = 69.6$ km s $^{-1}$ Mpc $^{-1}$, $\Omega_\Lambda = 0.714$, and $\Omega_m = 0.286$ and use Ned Wright’s Javascript Cosmology Calculator website (Wright 2006). In our adopted cosmology we use a conversion of 7.31 pc to 1 mas.

2. 5 GHZ LIGHT CURVE ANALYSIS

Light curves can indicate evidence of blazar-like behavior. Rapid variations can be used to estimate the brightness temperature, T_b . Figure 1 shows the most densely sampled radio light curve that we could create. There are more archival data at 5 GHz (corresponding to 23.5 GHz in the quasar rest frame) than at other frequencies. If there is a blazar coexisting with strong, persistent

¹ <http://www.narrabri.atnf.csiro.au/calibrators/>

emission, it can be significantly variable at higher frequency such as 1.25 cm wavelength in the quasar rest frame (Tornikoski et al. 2001). Figure 1 illustrates the difficulties associated with the analysis. PKS 1351–018 has modest variation on the order of 5 – 10% of the background of a quiescent flux density of ~ 900 mJy. Yet, the uncertainty in the individual observations is 5 – 10%. The data for Figure 1 can be found in Appendix A.

In order to get access to a large volume of unpublished Very Large Array (VLA) data (in the time frame before ATCA data became available), we relied on the National Radio Astronomy Observatory (NRAO) VLA Archive Survey (NVAS) Images Pilot page². We downloaded calibrated visibility FITS files and performed a self-calibration of the phase. This is a bright source with no confusing nearby sources, which lends itself to successful self-calibration. In general, we do not know the history of these data-sets, for instance, the observer’s intent with respect to the science goals and the flux density accuracy goal or if accurate automated “bad data flagging” was implemented properly. For outlier data points (candidates for rapid change), we considered things such as image rms noise, signatures of phase noise or side-lobes in the images of this unresolved source and elevation above the horizon. For crucial, suspect data-sets, we had to reduce the data by hand and flag bad antennas and reprocess the images. In order to minimize these issues we chose to avoid early VLA images that were not already present in the literature. In the end, the most conservative flux density calibration uncertainty that we can choose is 10% in general (Lorant Sjouwerman³ private communication). Although looking at the scatter of the points, this might be too large for most observations. However, if we were able to ascertain (i.e. from published papers or direct contact with the principal investigator) that the data reduction proceeded without these potential issues, an uncertainty in the flux density measurements is 5% based on the VLA manual⁴ (see also Perley and Butler 2013). We did not find all these circumstances, since it is sometimes difficult to recreate the past. This seemed like a reasonable compromise, NVAS FITS files greatly reduce the time required to analyze a large volume of data at the expense of a larger uncertainty.

We also wanted to increase the density of the time sampling of the ATCA observations after 2007. There were numerous observations in projects C2898 (2014) and C2914 (2016). The reductions of these data were generously provided for the purposes of this paper by Jamie Stevens (ATCA Senior System Scientist). The dense data sampling highlights the gradual changes in the flux density. This was true even in the summer of 2016 when there was a large γ -ray flare (see Section 6).

With that qualifier on the large VLA uncertainty aside, note that there are not the recurring large abrupt changes in amplitude in Figure 1 that one sometimes observes with a blazar (Tornikoski et al. 2001; Hovatta et al. 2009). But, there is some modest slow variation in amplitude. We have superimposed a sine wave on the densely sampled data from 1988 to 2020 in order to draw one’s eye to the gentle waves of variability that seem to exist within the data set even though the error bars are of similar amplitude. We do not, in any way, suggest that there is periodic behavior. This is only a device to emphasize the subtle long term variations. We can crudely estimate changes (peak to peak) of ~ 140 mJy over time frames of ~ 8 yr. This crude estimate is adequate for our purposes. The time variable brightness temperature is estimated in Hovatta et al. (2009) as

$$T_b = 1.548 \times 10^{-32} \frac{\Delta S_\nu d_L^2}{\nu^2 t^2 (1+z)}, \quad (1)$$

² <http://archive.nrao.edu/nvas/read.shtml>

³ Contact person for NVAS

⁴ <https://science.nrao.edu/facilities/vla/docs/manuals/oss/performance/fdscale>

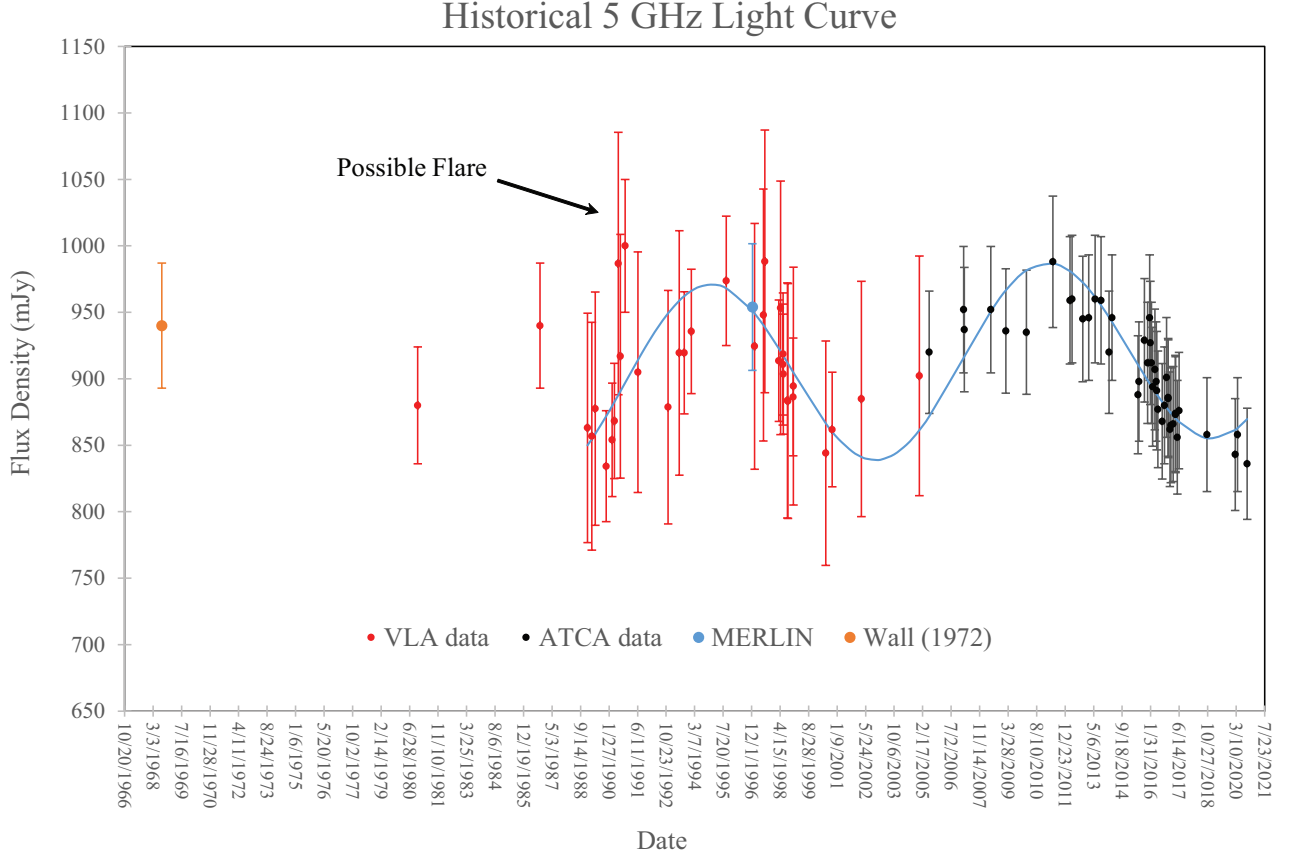


Figure 1. The highest density time sampling at any radio frequency is obtained at 5 GHz. The light curve is essentially in two halves, one is based primarily on VLA data and the latter half is based on ATCA data. This eliminates any perceived short term variability that is a consequence of absolute flux density calibration scales from different telescopes. We have verified in multiple epochs that the VLA flux density is consistently lower than the quasi-simultaneous ATCA flux density. There is a slow gradual variation that is visually highlighted by a sine curve with no physical meaning or statistical significance ascribed to it – only for a visual aid. There is also a sign of a flare in 1990. Flares are difficult to verify, since the measurement uncertainty is large enough to be consistent with enormous intrinsic flux density changes at this very high redshift. The MERLIN observation is described in Section 3.

where ΔS_ν (measured in Jy) is the change in flux density observed at frequency ν (measured in GHz) in a time frame t (measured in days in the observer’s frame) and d_L is the luminosity distance measured in meters. The slow wave modulation yields $T_b = 2.26 \times 10^{12}$ K. When $T_b > 10^{12}$ K, the inverse Compton catastrophe occurs. Most of the electron energy is radiated in the inverse Compton regime. The radio synchrotron spectrum from the jet is diminished in intensity to unobservable levels (Kellermann & Pauliny-Toth 1969). In order to explain the observed radio synchrotron jet in such sources, Doppler boosting is customarily invoked to resolve the paradox. The minimum Doppler factor, δ , required to avoid the inverse Compton catastrophe is (Hovatta et al. 2009)

$$\delta > \left[\frac{T_b}{10^{12} \text{ K}} \right]^{0.33} . \quad (2)$$

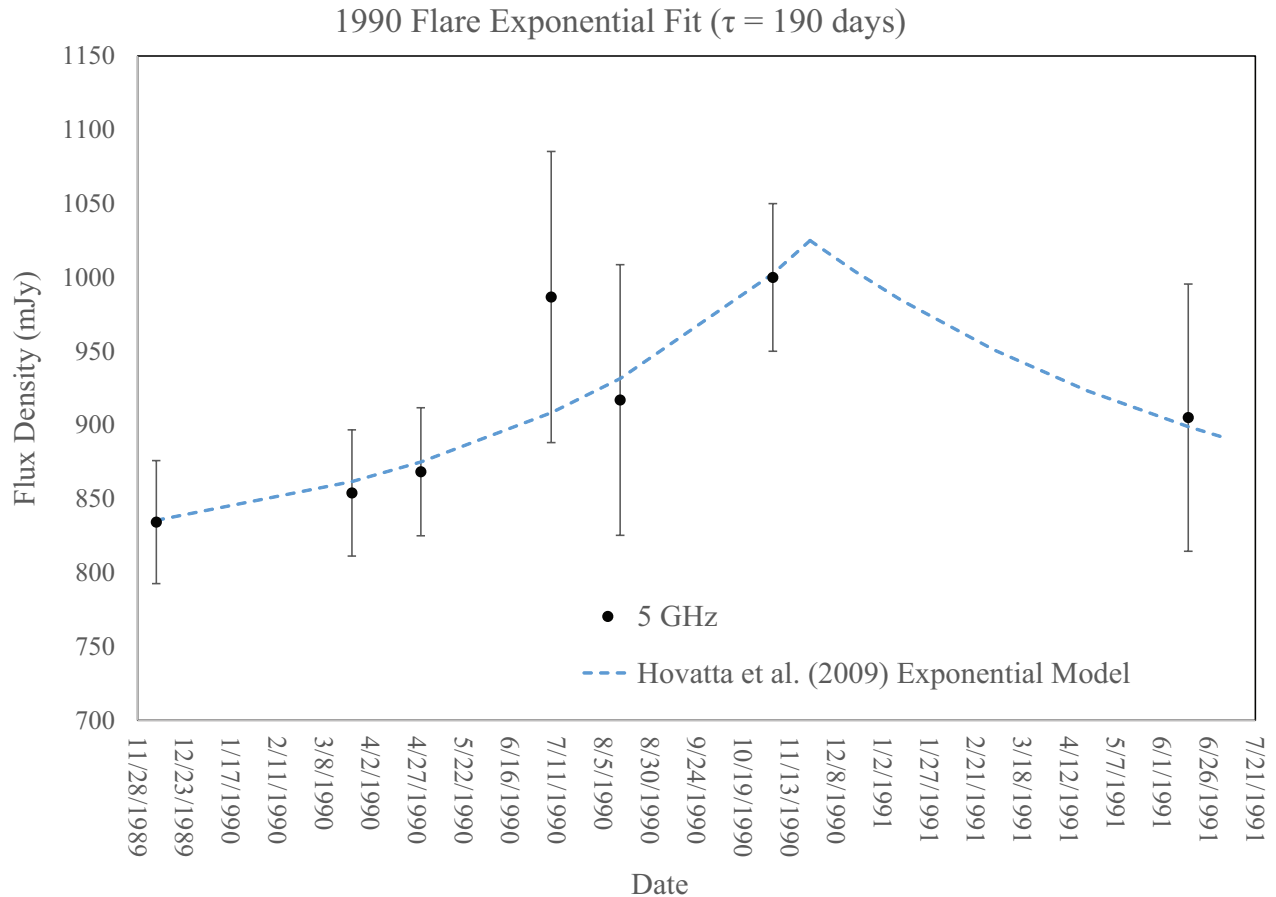


Figure 2. Evidence of a 5 GHz flare is presented in this closeup of the corresponding region in Figure 1. We fit the flux densities with a blazar flare model from the literature that is described in the text.

We note that slightly smaller values for the denominator ($T_b \sim 1 - 5 \times 10^{11}$ K) based on the equipartition assumption are often invoked (Readhead 1994). However, based on component sizes and flux density measured with Very Long Baseline Interferometry (VLBI) we estimate $T_b \approx 10^{12}$ K, in the next section on radio images. Furthermore, this paper does not assume equipartition in the jet, as we discuss in Section 8. From Equations (1) and (2), we get a bound of $\delta > 1.31$, not the kind of large Doppler factor expected for the strong γ -ray flare (Sahakyan et al. 2020).

The best evidence for a flare in Figure 1 is the indicated region during 1990. This requires a special consideration of the data in order to verify that this sparsely sampled event is not a manifestation of flawed observations or data reductions. We consider a magnified view of this region for a detailed analysis in Figure 2.

Before defining the flare, we noted that the 1990 August 14 data had 6 antennas for which the gain amplitude did not track the other 20 antennas, for whatever reason. The data were processed by hand by Lorant Sjouwerman instead of the automated NVAS routine. These antennas were flagged and the data reduction repeated based on the other 20 antennas followed by a phase self-calibration. Figure 2 indicates our best estimates of the flux density and uncertainty. We fit this with a blazar flare model developed in Valtaoja et al. (1999) and Hovatta et al. (2009). The authors successfully

describe flares by an exponential rise followed by an exponential decay with a time constant 1.3 times the time constant of the rising phase. We fit the data by finding the aforementioned model that minimizes the excess variance, Σ_{rms} , of the fit to the 7 data points that define the flare in Figure 2 (Nandra et al. 1997):

$$\Sigma_{\text{rms}}^2 = \frac{1}{N} \sum_{i=1}^N \frac{(S_i - f_i)^2 - \sigma_i^2}{f_i^2}, \quad (3)$$

where i labels one of the N measured flux densities, f_i is the expected value of this flux density from the Hovatta et al. (2009) model, S_i is the measured flux density and σ_i is the uncertainty in this measurement. The best fit is one that peaks on 1990 November 24 at 1025 mJy, corresponding to a flare peak of 225 mJy above the baseline. The time constant of the rise is $\tau = 190$ d. Hovatta et al. (2009) use $\tau = t$ in Equation 1. They also identify the flare peak (225 mJy in this case) with ΔS_ν in Equation (1). We formally interpret Equation (1) as the change in flux density in a time t . For $t = \tau$, the maximum ΔS_ν during the rise is $\Delta S_\nu = (1 - e^{-1}) 225 \text{ mJy} = 142 \text{ mJy}$. This yields $\delta > 8.1$ from Equation (2).

This minimum value of Doppler factor, δ_{min} , can be used to restrict the line of sight (LOS) to the emitting region of the jet. First, we express the Doppler factor in terms of kinematic quantities,

$$\delta = \frac{\gamma^{-1}}{1 - \beta \cos \theta}, \quad \gamma^{-2} = 1 - \beta^2, \quad (4)$$

where β is the normalized three-velocity of bulk motion, the associated Lorentz factor is γ , and θ is the angle of the motion to the LOS to the observer (Lind and Blandford 1985). For each value of δ_{min} , one can vary β in Equation (4) to find the maximum value of θ , $\theta_{\text{max}}\{\delta_{\text{min}}[(T_b)]\}$, that is compatible with δ_{min} (Ghosh and Punshly 2007):

$$\theta_{\text{max}}\{\delta_{\text{min}}[(T_b)]\} = \text{Max}_{|\beta|} \left(\arccos \left\{ \left[1 - \left(\frac{\sqrt{1 - \beta^2}}{\delta_{\text{min}}[(T_b)]} \right) \right] \beta^{-1} \right\} \right). \quad (5)$$

From the flare model and Equation (5) we conclude that

$$\theta_{\text{max}} = 7.1^\circ. \quad (6)$$

Comparing Figures 1 and 2, we draw the following conclusion. There is a blazar-like emission region. However, it is superimposed on the background of a much more luminous mildly variable component. This could be emission from a very luminous sub-kpc scale jet for which δ is far less than in the blazar-like region either due to a strong decelerating force and/or a change in the jet propagation direction relative to the LOS. The analysis of the radio images in the next section can potentially elucidate these circumstances. The apparent lack of many clear instances of blazar-like flares in Figure 1 (only the one in 1990 in Figure 2) is amplified by the time dilation due to the large redshift. In the quasar rest frame, 1989–2020 is only 6.6 years.

3. RADIO IMAGE ANALYSIS

The first radio image that we considered was the 1.4 GHz VLA observation in A-array which found an unresolved core (Neff and Hutchings 1990). In the absence of diffuse large scale emission we looked

Table 1. Gaussian Fits to S-Band VLBI Observations

Date	Component	Flux Density (mJy)	r (mas)	Position Angle (°)	FWHM (mas)	Axial Ratio (PA)	T_b K
1997 Jan 11	Core	880 ± 88	0	1.1	0 (-53°)	8.67×10^{11}
	North Lobe	30 ± 13	11.6 ± 1.7	-6	6.1	1	8.76×10^8
2002 Jul 24	Core	766 ± 77	0	...	1.0	1	8.39×10^{11}
	North Lobe	34.5 ± 13.8	11.9 ± 1.1	-9.7	6.6	1	8.50×10^8
2014 Aug 9	Core	787 ± 79	0	...	1.1	1	7.33×10^{11}
	North Lobe	32.6 ± 13.0	12.4 ± 1.7	-11.3	4.8	1	1.54×10^9

for compact structure on kpc scales. First, we imaged the deepest 5 GHz VLA A-array observation, project AB0560 (1990 March 23, one of the data points in Figure 2). Again, it was an unresolved nucleus. We then looked at the most sensitive 5 GHz observation with the Jansky Very Large Array (JVLA) in the A-array, project 16B-130 on 2016 December 3. Matt Smith kindly reduced the data he observed and created an image also showing nothing but an unresolved core. So we went to higher resolution looking for structure, by searching the Multi-Element Radio Linked Interferometer (MERLIN) archives for 5 GHz observations. Anita Richards generously provided the image FITS file of the one observation, on 1996 December 1, revealing an unresolved core. The restoring beam size was $69 \text{ mas} \times 52 \text{ mas}$ at a position angle $\text{PA} = 39^\circ$. Thus, we have an upper bound on the source size that is quite small. Thus motivated, we explore the VLBI observations of this source to look for the structure on scales less than 50 mas.

3.1. S-band VLBI

The Astrogate VLBI FITS image database⁵ contains calibrated VLBI 2.3 GHz data from numerous epochs from 1994 to 2020. Most of the observations use the 10 station Very Long Baseline Array (VLBA). However, from 1998–2003, the Research and Development VLBA project employed additionally up to 10 other antennas in order to create a global VLBI network (Petrov et al. 2009; Pushkarev and Kovalev 2012). The addition of the southern hemisphere stations and the multiple short scans in 24-h long observing sessions provide the best (u, v) coverage and resolution of any of the observations in the Astrogate VLBI FITS image database. The observation in Figure 3 from 2002 July 24 is of particular interest. The 2.3 GHz image was published in Pushkarev and Kovalev (2012). The 2002 image is the highest sensitivity, high resolution image available at S-band. The visibility data were fit with Gaussian brightness distribution components with an automated process. We re-analyzed the data with a manual data reduction for the purposes of this project. There is a prominent diffuse component to the north (which we will call the “North Lobe”). The details of the Gaussian fit are described in the second entry of Table 1. The method of defining measurement uncertainties can be found in Appendix B.

The brightness temperature in the last column is computed per the methods of Kellermann & Owen (1988):

$$T_b[\text{K}] = 1.22 \times 10^{12} (1+z) \frac{S_\nu}{\theta_1 \theta_2 \nu^2}, \quad (7)$$

⁵ <http://astrogeo.org>

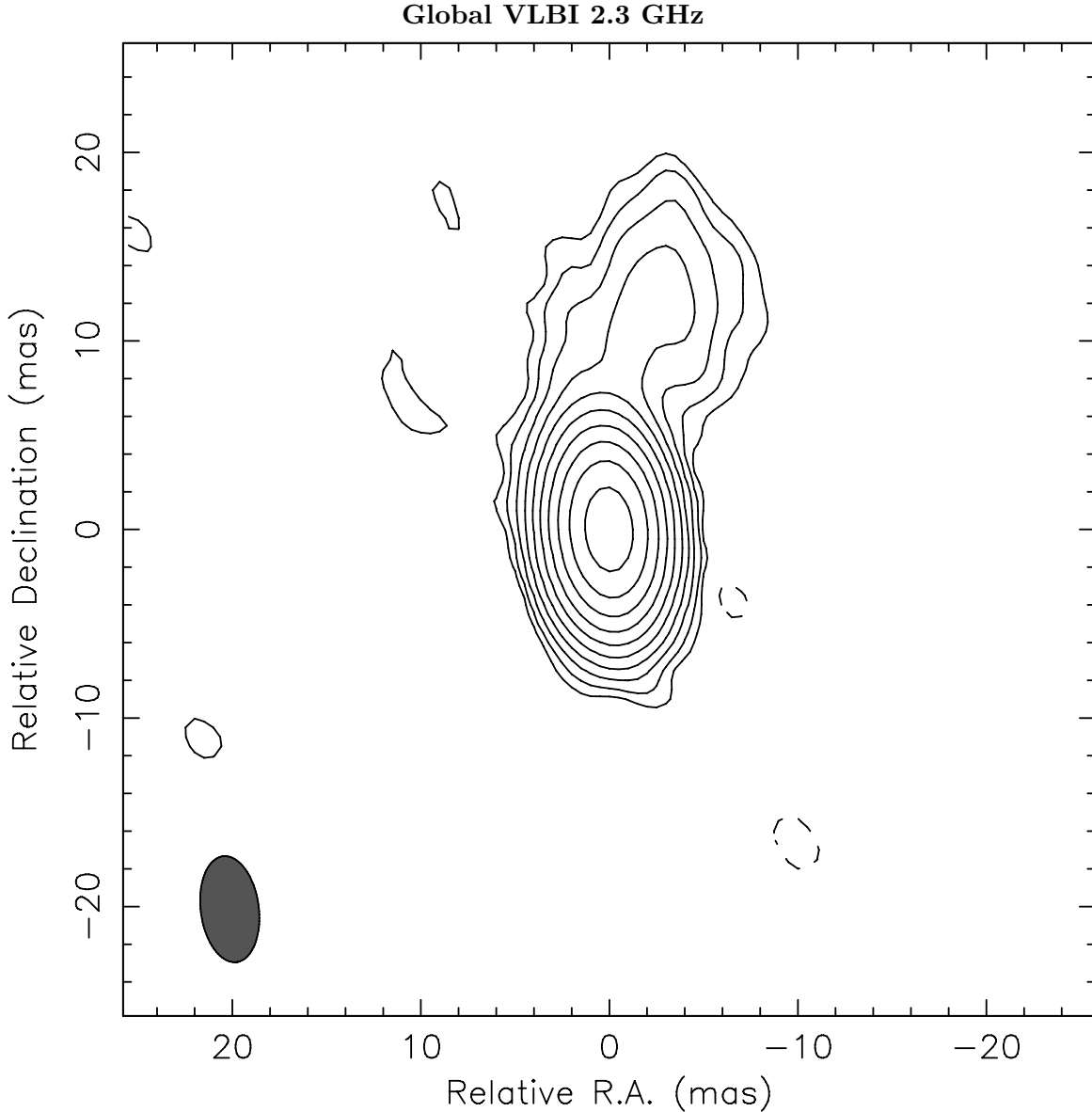


Figure 3. The Northern Lobe is very important to our estimate of the jet power. The best image of the feature is reconstructed using the S-band (2.3 GHz) global VLBI data taken on 2002 July 24. The peak intensity is $718 \text{ mJy beam}^{-1}$. The lowest level contour is $\pm 0.92 \text{ mJy beam}^{-1}$ and the positive contour levels increase by a factor of 2. The restoring beam is $3.08 \text{ mas} \times 5.66 \text{ mas}$ at $\text{PA} = 5^\circ$. The lobe appears to be at the end of a short, 11.5 mas jet. The lobe is resolved (fit with a Gaussian of FWHM of 6.6 mas from Table 1). It is comparable to the overall jet length projected on the sky plane. It is also unclear if there is a hotspot. It appears plume-like as opposed to an edge brightened morphology.

where ν is the observed frequency measured in GHz, θ_1 (θ_2) is the major (minor) axis of the elliptical Gaussian fitted full width at half-maximum (FWHM) measured in mas, and S_ν is the flux density of the component in Jy.

The earliest entry in Table 1 is a VLBA observation from 1997 January 11. It is composed of four 3-min scans spread out over two days to maximize (u, v) coverage. The fits are not carried out to

Table 2. 2.3 GHz VLBI Flux Density Compared to ATCA

Date	Telescope	Flux Density (mJy)	Reference
2018 Jan 18	VLBI	$970 \pm 97^{a,b}$	Astrogeo VLBI FITS image database
2018 Jan 22	ATCA	893 ± 45^c	ATCA Calibrator Database
2018 Jan 25	VLBI	$923 \pm 92^{a,b}$	Astrogeo VLBI FITS image database
2017 Dec 19 ^d	ATCA	881 ± 44^c	ATCA Calibrator Database

^aThe sum of the flux densities of the Gaussian fitted nucleus and North Lobe.

^b10% uncertainty (Homan et al. 2002; Pushkarev and Kovalev 2012).

^c5% uncertainty (Murphy et al. 2010).

^dAdditional data to corroborate the stability of the ATCA calibration in this time frame.

as many decimal points as our other fitted models (Fey and Charlot 2000). The North Lobe flux density is 0.03 Jy with no listed uncertainty. Thus, there is an additional uncertainty due to roundoff errors. We also found another image in the Astrogeo VLBI FITS image database with far less dense coverage in the (u, v) plane than the 2002 July 24 image that showed the northern lobe prominently (2014 August 9). The (u, v) coverage was fortuitous and the beam shape is not too elongated as in many epochs. The results of the Gaussian fitting process are listed as the third entry in Table 1. The lobe flux density is probably the same within uncertainty ($\sim 15 - 20\%$), but the smaller component size indicates that some diffuse emission was not captured by the sparse (u, v) coverage. There is strong evidence in Table 1 that the North Lobe was stable within VLBI uncertainties for at least 17 years.

Since these are very high resolution observations, we are interested to know how much flux density outside of the unresolved core was missed by the VLBI observations. In order to assess this and being cognizant of possible temporal variability of the core, we looked for quasi-simultaneous ATCA or VLA observations and VLBI observations. The VLBI absolute flux density calibration is less robust based on comparing the scatter of the C-band VLBI flux density to the light curve in Figure 1. Thus, it is very desirable to have two quasi-simultaneous VLBI observations with at least one ATCA or VLA observation at the same epoch. We could not find this circumstance in any of the VLBI bands except for S-band. Table 2 shows the only robust comparison that we could make based on archival data.

Table 2 seems to indicate that all of the flux density is contained within the VLBI components of the nucleus and North Lobe. If there were a few mJy resolved out of the North Lobe by the VLBI observations, we cannot confirm or reject this based on the uncertainties of the data in Table 2. We conclude that there is likely no measurable emission between the $\sim 50 - 60$ mas limit from MERLIN and the ~ 15 mas VLBI structure. We assume this to be the case in the remainder of the paper, up to the uncertainty in the flux density.

3.2. C-band VLBI

There are more VLBI data at C-band than any other frequency band. We were able to find 6 observations with useful data for our purposes. The relevant details are listed in Table 3. The third column, the restoring beam size, is very important since PKS 1351–018 displays a resolution dependent morphology (Frey et al. 2002). The beam position angle is not listed (to save space for more relevant details) as it is always nearly north-south within 15° . All of the data were fit by us

except for the O’Sullivan et al. (2011) data which is from the literature. We refit the Frey et al. (1997) (u, v) data with circular Gaussian models and multiple nuclear components, so it matches our data reduction technique for the four more recent data that were fit. The models are fit based on four detected components. As in Figure 3, the two most prominent features are the bright nucleus and the diffuse North Lobe. There is also a knot in the northern jet (that is prominent in Figure 4) as well as a Southeast Component that is very close to the nucleus (see Figure 5). The features that are recovered in the fitting process in the (u, v) plane depend on the resolution and sensitivity of the observations.

The main purpose of Table 3 is to track the location of the North Lobe over time (columns 6 and 7). In terms of (u, v) coverage, the four early observations are far superior to the last two from the Astrogro VLBI FITS image database. Surprisingly the 2014 February 18 Astrogro observation had much more sensitivity to the North Lobe emission than the other two observations from the Astrogro VLBI FITS image database (see Figure 4). The image is from segment BP177I of the 8th VLBA Calibrator Survey (VCS8) campaign (Petrov 2021). The source was used as an amplitude calibrator and it was observed in one scan on 2014 February 18 that achieved superior dynamic range compared to the other epochs⁶.

Compare the 2001 January 23 VLBI Space Observatory Program (VSOP) observation (Frey et al. 2002) with 10 stations of VLBA plus the *HALCA* satellite (the second entry in Table 3) restored with natural weighting with the best Astrogro observation from 2014 February 18 in Figure 4. The North Lobe position and flux density is very stable over 13 years. There is a faint jet connecting the nucleus to the lobe. In the right hand frame, this jet seems to begin at a small brighter protrusion of the nuclear contours almost directly northeast of the core. This is the component “Knot in North Jet” in Table 3. Based on Table 3 and Figure 4, due to the positional change from 2001 to 2014, this feature might be different faint knots in 2001 and 2014. The apparent bending of the jet to the east from 2001 to 2014 might be an indication that there is relativistic motion (Doppler aberration) in this region of the jet.

At higher resolution, at C-band, as well as at higher frequency (the next subsection), the diffuse radio emission of the North Lobe is resolved out. However, more compact features are revealed. The left hand frame of Figure 5 is lifted from Frey et al. (2002) and represents the same data as in the left hand side of Figure 4, but a higher resolution image is made using optimally weighted data on space-ground baselines to enhance angular resolution. The North Lobe and the Knot in North Jet are resolved out, but a “Southeast Component” is revealed. The absolute flux density calibration with VSOP is difficult, but we estimate ≈ 40 mJy in the Southeast Component. In order to validate its existence, we present a global VLBI – VLBA plus 6 European VLBI Network (EVN) telescopes – image from a 24-h observation of O’Sullivan et al. (2011) from 2000 June 5, only 7 weeks earlier in the quasar rest frame. The image in the right hand frame of Figure 5 was generously created for the purpose of this study by Shane O’Sullivan. The Gaussian fitted component FWHM from Table 3 are represented by circles and ellipses with crosses. These components seem to capture every observed feature including the North Lobe. There is a strong component to the southeast as well as a very weak compact component to the northeast, the putative knot in the northern jet. The locations do not line up perfectly with VSOP, but that might be an artifact of trying to fit features

⁶ Leonid Petrov private communication

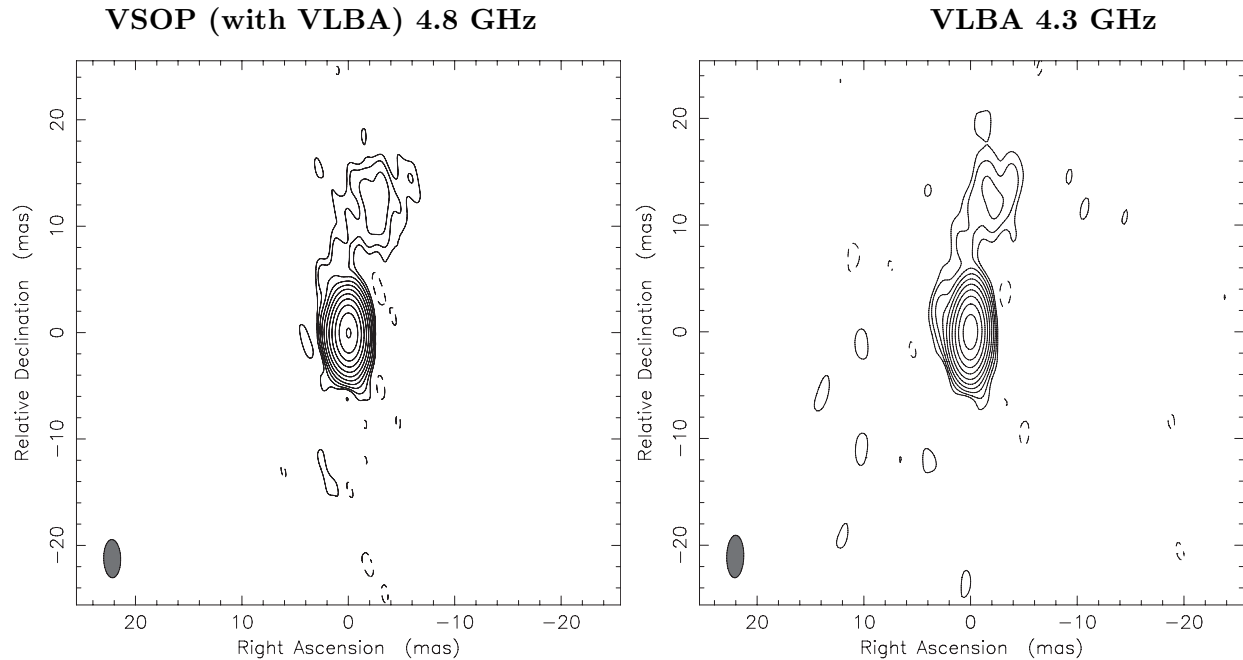


Figure 4. This figure compares the 4.8 GHz VSOP (including the VLBA) observation from 2001 January 23 (left) with the 4.3 GHz VLBA observation from 2014 February 18 (right). The latter observation has far less time on the source, however the two images separated by 13 years look remarkably similar. There are no measurable changes to the North Lobe within measurement uncertainties as evidenced by Table 3. In the left image, the peak intensity is $641 \text{ mJy beam}^{-1}$, the lowest level contour is $\pm 0.6 \text{ mJy beam}^{-1}$. The restoring beam is $1.6 \text{ mas} \times 3.59 \text{ mas}$ at $\text{PA} = 1.3^\circ$. In the right image, the peak intensity is $769 \text{ mJy beam}^{-1}$, the lowest level contour is $\pm 0.955 \text{ mJy beam}^{-1}$. The restoring beam is $1.59 \text{ mas} \times 3.99 \text{ mas}$ at $\text{PA} = -1.5^\circ$. The positive contour levels increase by a factor of 2.

on scales smaller than the synthesized beam. This might also explain the flux density difference in the Southeast Component ($79 \pm 15 \text{ mJy}$ versus $40 \pm 10 \text{ mJy}$). Other contributing factors could be extreme variability and the absolute flux density calibration of VSOP. In this context, it should be noted that we were unable to retrieve all of the original files used in the VSOP data reduction. Hence, there is some uncertainty in the absolute flux density calibration in the files we could retrieve. There is a possible difference with the calibration of Frey et al. (2002) that indicates $\approx 40 \text{ mJy}$ in the Southeast Component, we fit 31.2 mJy using the data files that were found. However, it is still consistent within the uncertainties in Table 3. We investigate this component further with higher frequency VLBI in the next subsection.

The primary objective of the C-band Gaussian fits in Table 3 is to quantify the apparent motion of the North Lobe. Hence, we have included some Astrogateo data that likely have insufficient sensitivity to capture the diffuse lobe flux density accurately. However, they are adequate for finding the position of the North Lobe. Based on Table 3 and Figure 4, it seems to be stationary over a quarter century within uncertainties. Any apparent motion of the Northern Lobe is masked by the relatively large uncertainties. These uncertainties control the constraints that we can put on an upper bound to the component motion. Figure 6 is a scatter plot of the separation versus time from the Gaussian fits in Table 3. The separation data in Table 3 were fit by least squares with uncertainty in the vertical variable in Figure 6 (Reed 1989). The standard error of the fit is given by the dashed lines. Based

VSOP (with VLBA) 4.8 GHz

Global VLBI 5.0 GHz

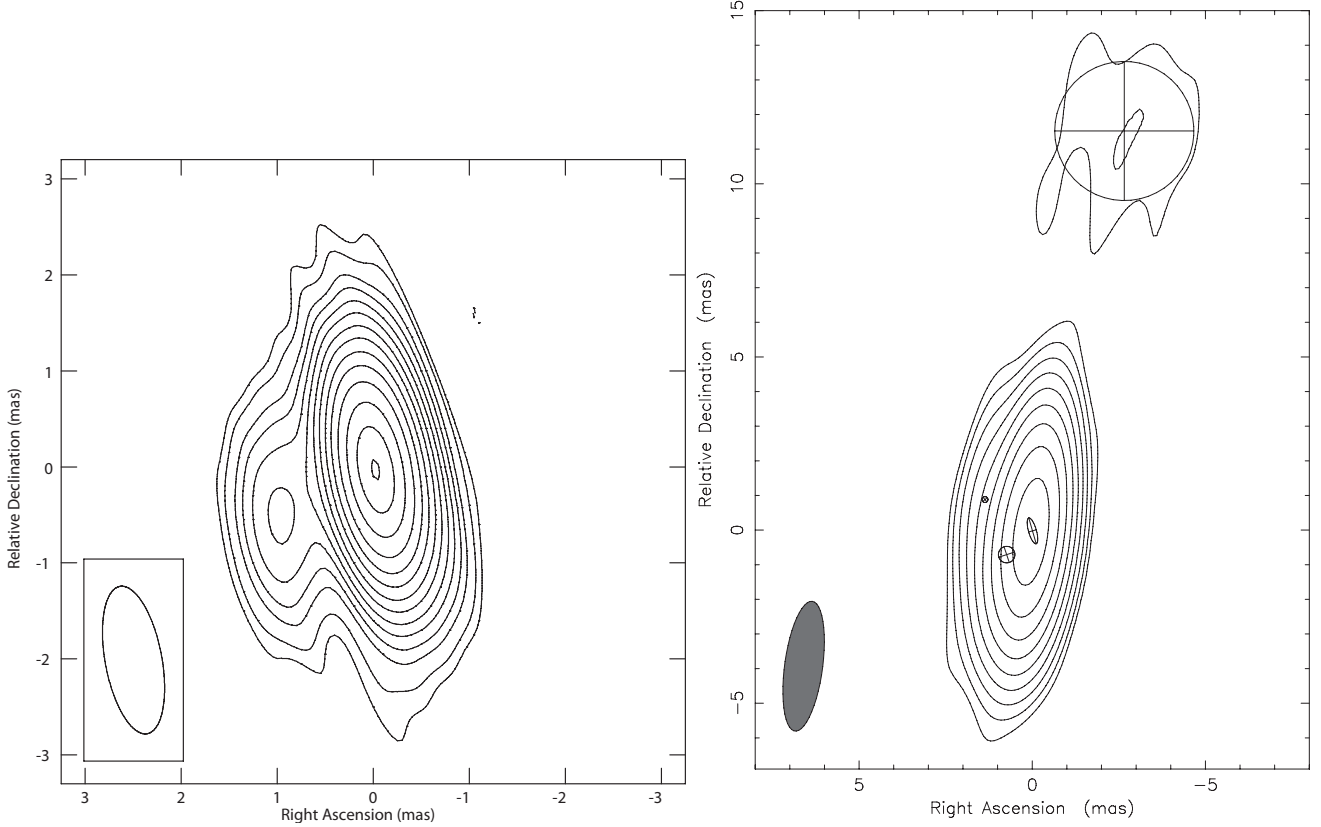


Figure 5. On the left is the 4.8 GHz VSOP image from 2001 January 23, with special weighting to enhance the space-ground baseline data, as reproduced from (Frey et al. 2002). Contours are at $-1, 1, 1.5, 2.5, 3.5, 5, 7, 10, 14, 20, 28, 40, 56, 80,$ and 99% of the peak brightness of $547 \text{ mJy beam}^{-1}$. The restoring beam is $0.59 \text{ mas} \times 1.56 \text{ mas}$ at $\text{PA} = 11^\circ$. The image on the right hand side is a 5 GHz global VLBI image from 2000 June 5. The peak intensity is $663 \text{ mJy beam}^{-1}$, the lowest level contour is $\pm 1.66 \text{ mJy beam}^{-1}$. The restoring beam is $1.1 \text{ mas} \times 3.78 \text{ mas}$ at $\text{PA} = -7.6^\circ$. The positive contour levels increase by a factor of 2. The ellipses with crosses are the Gaussian components from Table 3. Note that both observations detect a Southeast Component.

on the fit, the lobe advances at $0.006 \pm 0.018 \text{ mas yr}^{-1}$, i.e. consistent with no motion. In our chosen cosmology, we have 7.31 pc mas^{-1} , so the apparent velocity of the North Lobe relative to the nucleus is $v_{\text{apparent}} = (0.13 \pm 0.44) c$. The uncertainties in the data do not allow us to provide much more than an upper bound of $v_{\text{apparent}} < 0.57 c$.

3.3. High Frequency VLBI

High frequency VLBI observations have the resolution required to define the Southeast Component. The details of the four high frequency observations are described in Table 4. The first observation is the X-band observation performed simultaneously with the first S-band entry in Table 1 (Fey and Charlot 2000). The second observation to consider is the global VLBI X-band observation

Table 3. Gaussian Fits to C-Band VLBI Observations

(1) Date	(2) Array/ Frequency	(3) Restoring Beam (mas)	(4) Component	(5) Flux Density (mJy)	(6) r (mas)	(7) Position Angle ($^{\circ}$)	(8) FWHM (mas)	(9) Axial Ratio/PA	(10) T_b (K)	(11) Ref.	
1995 Jan 28	VLBA 5 GHz	4.9×2.0	Core	919 ± 92	0	...	0.57	1	6.50×10^{11}	<i>a,b</i>	
			North Lobe	14.0 ± 5.6	12.4 ± 0.8	-11.8	2.51	1	5.11×10^8	<i>b</i>	
			Knot in North Jet	not detected	<i>b</i>
			Southeast Component	22.4 ± 7.1	1.6 ± 0.3	131.0	0.05^c	1	...	<i>c</i>	<i>b,d</i>
2000 Jun 5	Global VLBI 5 GHz	3.51×1.10	Core	681 ± 68	0	...	0.77	$0.3/-164^{\circ}$	8.91×10^{11}	<i>g</i>	
			North Lobe	16.8 ± 6.7	11.9 ± 0.7	-12.9	4.02	1	2.42×10^8	...	
			Knot in North Jet	14.3 ± 6.2	1.6 ± 0.3	56.6	<i>c</i>	<i>c</i>	...
			Southeast Component	78.5 ± 14.5	1.0 ± 0.5	132.7	0.48	1	7.88×10^{10}	...	
2001 Jan 23 ^e	VSOP 4.8 GHz	3.59×1.60	Core	664 ± 66	0	0	0.46	1	7.83×10^{11}	<i>f,b</i>	
			North Lobe	14.1 ± 5.6	12.5 ± 0.7	-11.0	3.93	1	2.28×10^9	<i>b</i>	
			Knot in North Jet	4.0 ± 3.0	5.2 ± 0.3	67.0	<i>c</i>	<i>c</i>	<i>b</i>
			Southeast Component	32.1 ± 8.5	1.3 ± 0.3	113.0	0.05^c	1	...	<i>c</i>	<i>b</i>
2001 Jan 23 ^e	VSOP 4.8 GHz	1.56×0.59	North Lobe	not detected	detected	<i>b</i>	
			Southeast Component	40 ± 10	1.3 ± 0.3	113.0	<i>c</i>	<i>c</i>	<i>b</i>
2014 Feb 18	VLBA 4.3 GHz	3.99×1.59	Core	802 ± 80	0	...	0.49	1	1.04×10^{12}	<i>h,b</i>	
			North Lobe	13.3 ± 5.3	12.6 ± 0.8	-12.4	2.04	1	9.93×10^9	<i>b</i>	
			Knot in North Jet	8.5 ± 4.3	5.7 ± 0.7	18.9	0.68	1	5.71×10^{10}	<i>b</i>	
			Southeast Component ^d	33.1 ± 8.4	1.4 ± 0.3	106.9	0.01	1	...	<i>c,d</i>	<i>b</i>
2016 Feb 17	VLBA 4.3 GHz	4.08×1.66	Core	656 ± 66	0	...	0.55	1	6.27×10^{11}	<i>h,b</i>	
			North Lobe ⁱ	9.6 ± 3.8	12.8 ± 0.8	-13.2	1.53	1	...	<i>i</i>	<i>b</i>
			Knot in North Jet ^d	7.1 ± 3.3	6.0 ± 0.7	15.6	0.34	1	...	<i>c,d</i>	<i>b</i>
			Southeast Component ^d	19.7 ± 5.5	1.5 ± 0.4	114.0	0.04	1	...	<i>c,d</i>	<i>b</i>
2018 Dec 1	VLBA 4.3 GHz	3.81×1.42	Core	699 ± 70	0	...	0.46	1	9.76×10^{11}	<i>h,b</i>	
			North Lobe ⁱ	11.0 ± 4.4	12.0 ± 0.5	-13.5	1.66	1	...	<i>i</i>	<i>b</i>
			Knot in North Jet ^d	13.9 ± 4.9	5.4 ± 0.7	19.1	0.01	1	...	<i>c,d</i>	<i>b</i>
			Southeast Component ^d	46.0 ± 9.0	1.4 ± 0.4	118.2	0.06	1	...	<i>c,d</i>	<i>b</i>

^aFrey et al. (1997)^bThis paper^cEffectively a point source, T_b estimate ill-defined^dVery poor long baseline (u, v) coverage, fit parameters may not be robust.^eSee the text description of the absolute flux density uncertainty of our results. The second entry for this observation is from the image in Frey et al. (2002) with preferential weighting to the long space-Earth baselines.^fFrey et al. (2002)^gO’Sullivan et al. (2011)^hPetrov (2021), Astrogro VLBI FITS image databaseⁱ(u, v) short baseline coverage is degraded relative to 2014 February 18, much of the North Lobe flux density is missing. The true uncertainty cannot be estimated.

that was coincident with the S-band observation described in Table 1 and Figure 3. The most curious feature is that the elongated core seen in the global VLBA observation of 2000 June 5 is resolved into a nuclear two component structure. There was an observation at 8.4 GHz with high background noise that we do not include in the table from 2000 June 5 (O’Sullivan et al. 2011).

The two never before published observations from the VLBA archives are presented in Figure 7. First of all, note that the three observations and the 2000 June 5 global VLBI observations at 5 GHz define a consistent axis for the nuclear region at PA $\approx -165^{\circ}$ and based on the X-band resolution, it is directed toward the south. This explains the jet geometry. The inner jet is directed at PA $\approx -165^{\circ}$

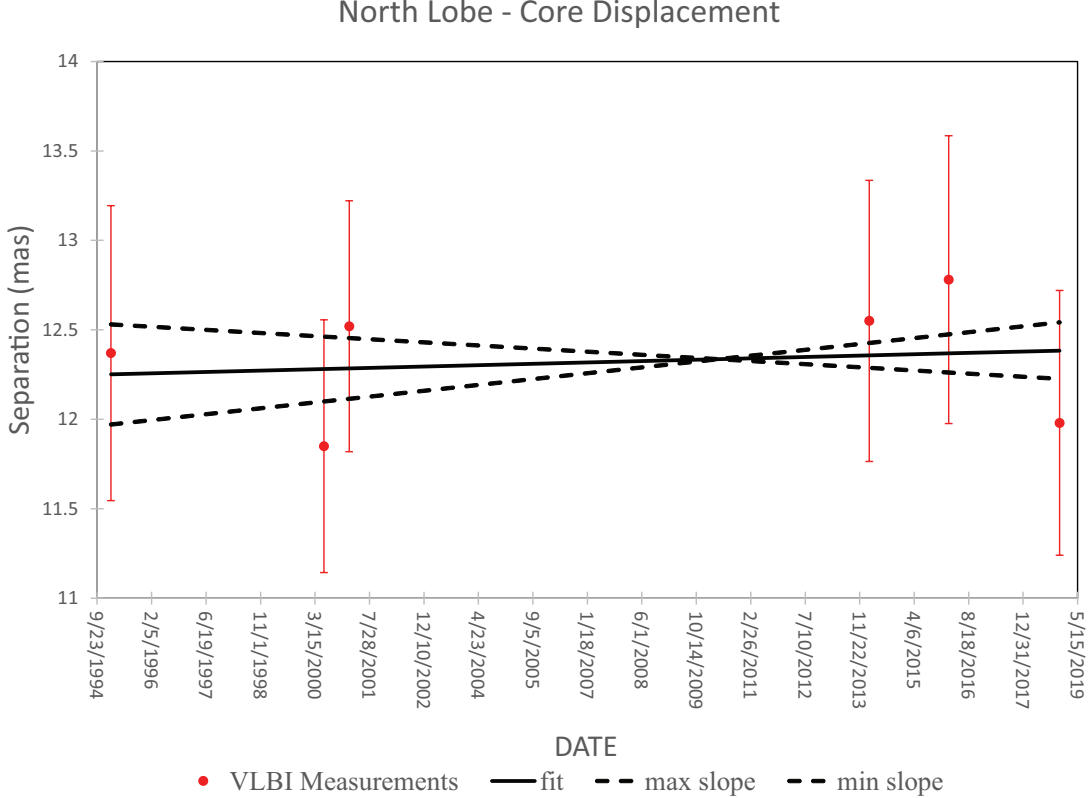


Figure 6. There is formally no motion detected in the Northern Lobe in our 6 measurements of its position over 23 years. Due to the high redshift, the instrumental uncertainties correspond to relatively large physical uncertainties in the true position thereby masking any slow motion. We try to bound the motion with a fit to the data with uncertainty in the vertical variable (Reed 1989). The fit is the solid line and the standard error of the fit is indicated by the dashed lines. The maximum apparent velocity that is compatible with the standard error is $v_{\text{apparent}} < 0.57 c$.

for about 0.8 mas. At this point it veers abruptly toward the Southeast Component at PA $\approx 130^\circ$ (an $\approx 65^\circ$ rotation). We postulate that after which it bends toward the north through the Knot in North Jet (3–5 mas out), finally terminating at the North Lobe (12.5 mas out). Such behavior up to and through the Southeast Component is indicative of Doppler aberration and a nearly polar LOS (Lind and Blandford 1985).

Next, we use the high frequency observations to gain clues into the nature of the Southeast Component. The lack of a detection at 22.4 GHz is unexpected based on the apparent sensitivity of the observations. The 9-h observation for VLBA project BN0003 during 1996 September 7–8 produced a total of 64 minutes of data on source PKS 1351–018 with 32 MHz bandwidth in a single polarization. The phased-VLA (in D-array) was added to the array improving the (still sparse) u, v coverage and improving the sensitivity. We found an rms noise of $\approx 1.5 \text{ mJy beam}^{-1}$. Based on the size found at 15 GHz in Table 4, we would have expected to have detected a flux density as low as 7.5 mJy at the 5σ level. Figure 8 shows extrapolated power law fit from the lower frequency data. We expected 10–15 mJy. There are three possible explanations:

Table 4. Gaussian Fits to High Frequency VLBI Observations

(1) Date	(2) Array/ Frequency	(3) Restoring Beam (mas)	(4) Component	(5) Flux Density (mJy)	(6) r (mas)	(7) Position Angle ($^{\circ}$)	(8) FWHM (mas)	(9) Axial Ratio/PA	(10) T_b (K)	(11) Ref.
1997 Jan 11	VLBA 8.55 GHz	2.2×1.0	Core	480 ± 48	0	...	0.50	$0/24^{\circ}$...	^a
			North Lobe	not	detected
			Southeast Component ^c	30 ± 9.3	1.0 ± 0.3	135	0.9	$0/30^{\circ}$
2002 Jul 24	Global VLBI 8.65 GHz	1.75×0.79	Core	466 ± 46	0	...	0.18	1	1.07×10^{12}	^b
			North Lobe	11.8 ± 4.7	11.5 ± 0.3	-20.6	2.1	1	2.62×10^9	^e
			Nuclear Secondary ^c	233 ± 23	0.65 ± 0.3	-166.6	0.33	1	1.64×10^{11}	^d
			Southeast Component ^c	37.9 ± 8.5	1.2 ± 0.3	141.0	^d	1
1996 Jun 13	VLBA 15.4 GHz	1.16×0.47	Core	529 ± 53	0	...	0.75	$0.19/17.6^{\circ}$	1.99×10^{11}	^e
			North Lobe	not	detected
			Southeast Component	17.4 ± 4.6	1.2 ± 0.2	145.0	0.0	
1996 Sep 7	VLBA 22.1 GHz	1.16×0.47	Core	398 ± 40	0	...	0.76	$0.22/18.7^{\circ}$	3.61×10^{10}	^e
			North Lobe	not	detected
			Southeast Component	< 7.5	

^aFey and Charlot (2000). Flux density error estimate of Southeast Component uses the 26% uncertainty computed in the 2002 observation added in quadrature with roundoff error.

^bPushkarev and Kovalev (2012)

^cSparse (u, v) coverage at baselines long enough to model the ~ 1 mas nucleus.

^dEffectively a point source, T_b estimate ill-defined

^eThis paper

1. There is a flaw in the radio observation introduced by a subtle calibration issue. Although there are no obvious signs of artefacts in the image, the surface brightness of the noise is 2.25 times higher at 22.1 GHz than at 15.4 GHz. We investigated this possibility by imaging 4C 39.25, a very bright source observed during the same observing run. We would expect that such an error would be easier to spot in those data. Nothing was apparent. Further, we imaged the PKS 1351–018 data using various subsets of the antennas, none of which indicated significant emission at the position of the Southeast Component, or significant changes in the observed morphology.
2. There could be strong synchrotron cooling that makes the spectrum curve downward sharply around 15 GHz.
3. The source might be highly variable. However, consider the following from Table 4. 18.5 days earlier in the quasar rest frame, the Southeast Component was detected with 22 mJy at 15.4 GHz. 20 days later in the quasar rest frame, it was detected with ≈ 30 mJy at 8.55 GHz (similar to the estimated flux density in 2002).

We simply do not have enough information to reach a definitive conclusion on the contribution of each of these possibilities. We assume that all of these are factors, the K-band image is relatively noisy, and there is a spectral steepening (perhaps not severe). Furthermore, there is some significant (but not extreme) variability. In Figure 8, we look at a scatter plot of the flux density at the four frequency bands in order to try and organize the trend in the difficult to measure quantity. A good measurement requires high resolution, high sensitivity, and high dynamic range. That being said, 15 GHz VLBA is our most reliable data. The only thing stopping a very tight trend in Figure 8 are

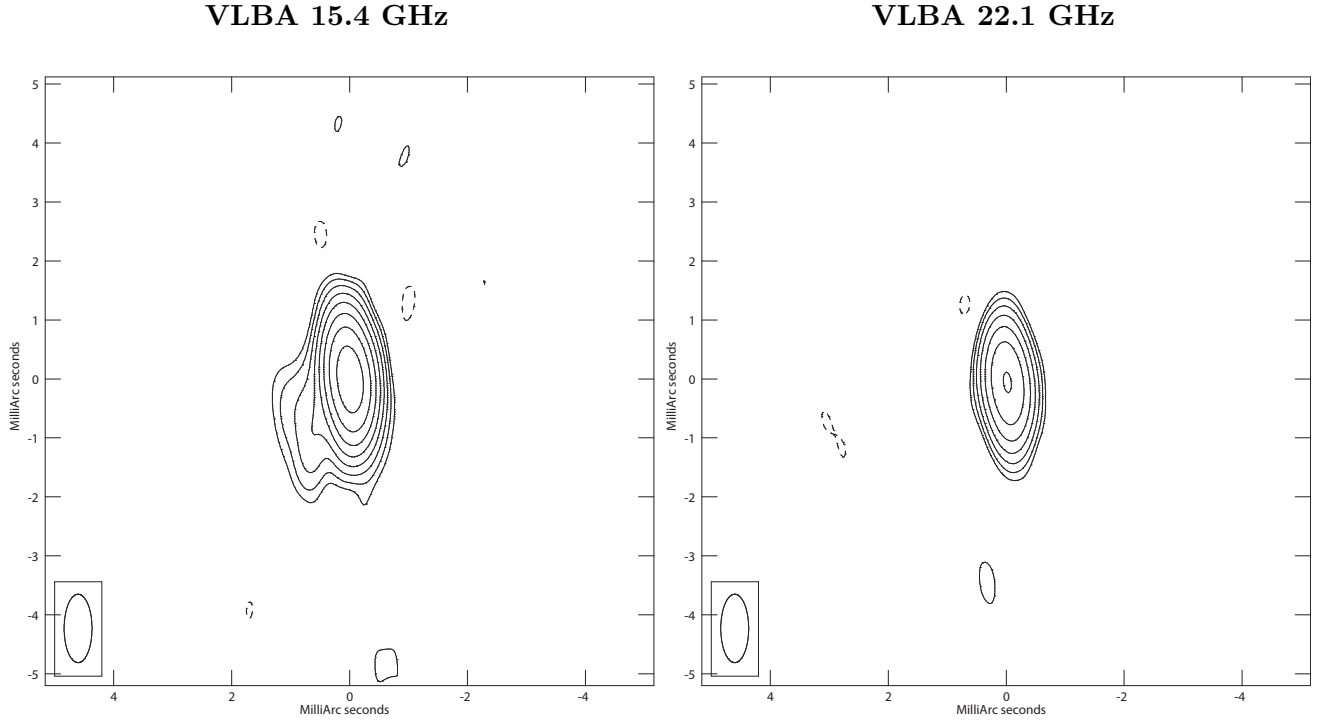


Figure 7. On the left hand side is the 15.4 GHz VLBA image from project BK0042 on 1996 June 13. On the right hand side is the 22.1 GHz VLBA image from 1996 September 7. To aid comparison, both images are created with the same restoring beam, the naturally weighted beam from the 15.4 GHz observation, $1.16 \text{ mas} \times 0.47 \text{ mas}$ at $\text{PA} = 1.9^\circ$. The bottom contour is ± 3 times the rms noise $1.95 \text{ mJy beam}^{-1}$ ($4.47 \text{ mJy beam}^{-1}$) and the peak intensity is $405 \text{ mJy beam}^{-1}$ ($298 \text{ mJy beam}^{-1}$) at 15.4 (22.1) GHz. The positive contours increase by factors of two. Even though the two observations occurred only 18.5 days apart in the quasar rest frame, the prominent Southeast Component seen in the left panel is absent in the right panel.

the two disparate C-band flux densities and the 22 GHz non-detection. The 22 GHz data are still a mystery considering the detections of the Southeast Component within 3 weeks before and after (in the quasar rest frame). In the following, we will assume that the power law fit in Figure 8 (spectral index $\alpha \approx 0.98$) applies to the data at frequencies below 15 GHz with some modest ($\sim 20 - 30\%$) variability.

4. THE SYNCHROTRON SPECTRAL ENERGY DISTRIBUTION

This section compiles the radio to millimeter wave data that are used to construct possible physical models of the radio source later in this paper. The results are in Table 5. Since the data have relatively large measurement uncertainty compared to the magnitude of flux density variability of PKS 1351–018, we have averaged the historical data to reduce the uncertainty. Figure 1 is the best example, but we also average at other frequencies when possible. For now, we simply collect the data and create a synchrotron SED that extends from $\nu \sim 6 \times 10^8 \text{ Hz}$ to $\nu \approx 10^{12} \text{ Hz}$ in the quasar rest frame.

The first column of Table 5 is the observed frequency. This is converted into the logarithm of the frequency in the quasar rest frame in the next column. We then give the flux density with its uncertainty which is considerable at very low and very high frequencies for individual measurements.

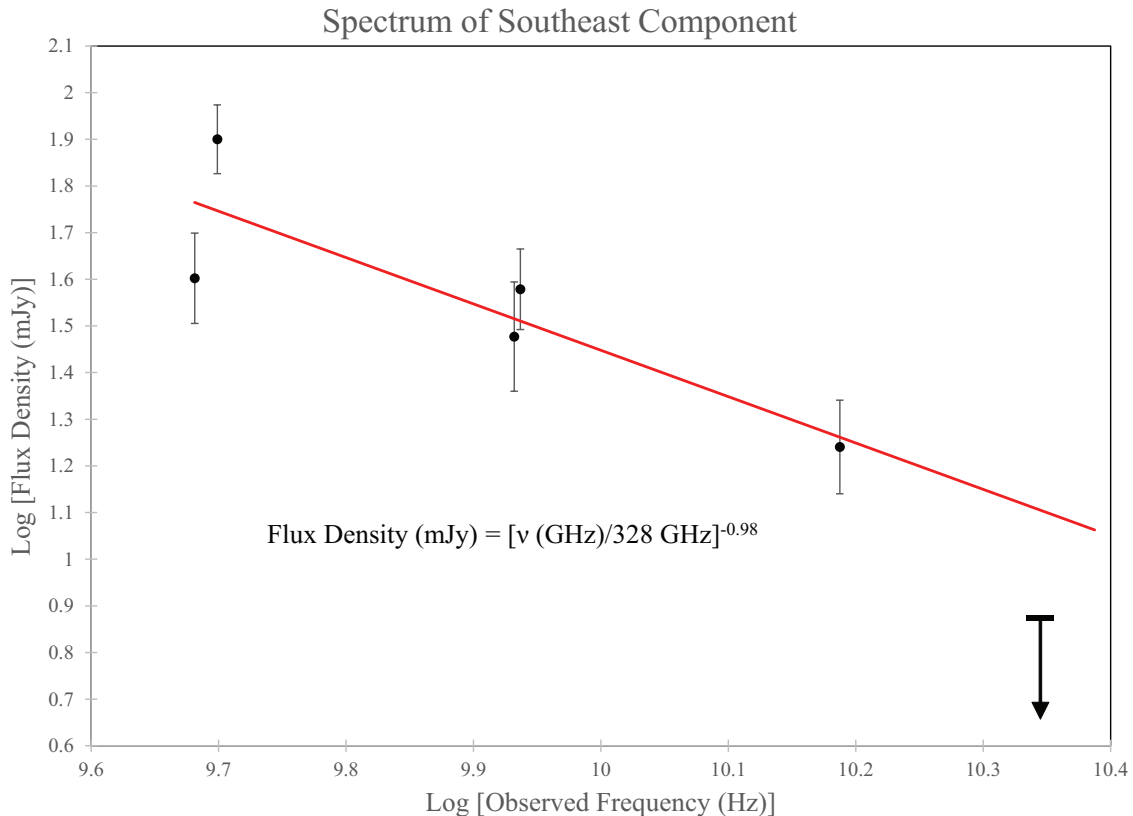


Figure 8. Based on all the available observations, this is our chosen characterization of the spectrum of the Southeast Component. It is a component only 1 mas from the core and only $\sim 3 - 5\%$ as bright. It is apparently variable as well, but this magnitude is difficult to determine as a result of the uncertainty of fitting a relatively faint component so close to a bright core. Variations on the order $\pm 30\%$ seem consistent with the scatter to the fit of the data from 4.8 to 15.4 GHz. The spectral fit is therefore, an average fit and it is clearly steep. We use the spectral index of $\alpha = 0.98$ in our theoretical models of the source. Our estimates of jet power do not rely strongly on this quantity. We also note that there might be a spectral turnover at ≈ 15 GHz.

We then list the telescope used, the reference to the data and the comments in the final three columns. We note how many of the frequencies were able to be averaged over at least a modest set of historical observations with the same telescope in the comments column. In our modelling, the low frequency data are very important. The $\nu_o = 107$ MHz to $\nu_o = 227$ MHz Galactic and Extra-galactic All-sky MWA survey (GLEAM) data are very useful, but have much scatter due to the low flux densities (ν designates frequencies in the cosmological rest frame of the quasar and ν_o the observed frequencies; $\nu = (1 + z)\nu_o$). There were 15 channels and we averaged 5 at a time in order to get a more robust flux density. Even so, the data do not agree well with the $\nu_o = 150$ MHz Tata Institute for Fundamental Research (TIFR) Giant Metrewave Radio Telescope (GMRT) Sky Survey Alternate Data Release (TGSSADR) flux density. The modest low frequency flux density of PKS 1351–018 provides a challenge to survey observations, and TGSSADR has only one data point, so it is more difficult to check its consistency. We also were fortunate to obtain numerous P-band observations from JVLA and the one from the VLA. At $\nu_o = 340$ GHz, we pick the mean and the standard deviation of 64 observations binned into 15 distinct epochs (each epoch has < 10 d spread in the observations

Table 5. Radio Data for PKS 1351–018

ν_o	$\log \nu$	Flux	Telescope	Reference	Comments
Observed	Quasar Rest	Density			
Frequency	Frame				
(MHz)	(Hz)	(mJy)			
123^{+20}_{-16}	8.76 ± 0.06	214.5 ± 27.8^a	MWA ^b	Wayth et al. (2015) ^c	5 bin average
150	8.76	185.0 ± 27.8^a	GMRT	Intema et al. (2017); Hurley-Walker (2017)	TGSSADR
165 ± 15	8.89 ± 0.04	246.4 ± 37.0^a	MWA ^b	Wayth et al. (2015) ^c	5 bin average
208 ± 19	8.99 ± 0.04	276.8 ± 41.5^a	MWA ^b	Wayth et al. (2015) ^c	5 bin average
330	9.19	329.7 ± 33	VLA	This paper	A-array
340	9.20	362 ± 50	VLA/VLITE	This paper, Clarke et al. (2016); Polisensky et al. (2016) ^d	15 epoch average
365	9.24	371 ± 37	Texas Interferometer	Douglas et al. (1996)	
960	9.66	510 ± 51	RATAN-600	Kovalev et al. (1999)	
1400	9.82	733 ± 37	VLA D-array	Condon et al. (1998)	NVSS
1400	9.82	709 ± 35	VLA B-array	Becker et al. (1995)	FIRST
1484	9.84	743 ± 37	VLA A-array	Neff and Hutchings (1990)	
2100	10.00	850 ± 85	ATCA	Calibrator Database ^e	
2700	10.10	897 ± 53	ATCA	Calibrator Database ^e	8 epoch average
4900	10.36	905 ± 42	VLA and ATCA	Average of Figure 1	
8470	10.60	812 ± 70	VLA	NVAS, this paper	27 epoch average
14900	10.85	669 ± 39	ATCA	Calibrator Database ^e	8 epoch average
22400	11.02	542 ± 35	ATCA	Calibrator Database ^e	8 epoch average
33000	11.19	373 ± 56	ATCA	Calibrator Database ^e	
43000	11.31	400 ± 80	VLA	Calibrator List ^f	
43000	11.31	303 ± 61	ATCA	Calibrator Database ^e	
43000	11.31	373 ± 56	ATCA	Calibrator Database ^e	
90000	11.63	177 ± 18	IRAM 30-meter	Steppe et al. (1995)	
93000	11.64	170 ± 50	ATCA	Calibrator Database ^e	
230000	12.03	65 ± 13	IRAM 30-meter	Steppe et al. (1995)	

^aUncertainty from Hurley-Walker (2017)

^bMurchison Widefield Array

^cGLEAM: <https://vizier.u-strasbg.fr/viz-bin/VizieR-3?-source=VIII/100/gleamegc>

^dVLA Low Band Ionospheric and Transient Experiment (VLITE). Data provided by Wendy Peters.

^e<https://www.narrabri.atnf.csiro.au/calibrators>

^f<https://science.nrao.edu/facilities/vla/observing/callist>

in the quasar rest frame) to be the values of the flux density and uncertainty, respectively. These observations span 5.5 yr from 2015 to 2020. The synchrotron SED is plotted in Figure 9. We added a log-parabolic fit. Unfortunately, the high frequency observations that define the peak are difficult and the uncertainty and scatter are larger than one would like. A carefully calibrated 43 GHz JVLA observation would be very useful. The SED peak is at $\nu_{\text{peak}} \approx 5 \times 10^{11}$ Hz. Based on the “blazar sequence” this is at the low end of the peak frequency expected for a flat spectrum *Fermi* detected quasar with a peak spectral luminosity of $\sim 2 \times 10^{46}$ erg s⁻¹ (Ghisellini et al. 2017). Typically, they find $\nu_{\text{peak}} \approx 2.0 \times 10^{12}$ Hz for a flat spectrum quasar that is *Fermi* detected. The integrated luminosity of the SED up to 10^{12} Hz in the quasar rest frame (the limit of our data) is 7×10^{46} erg s⁻¹, or $L_{\text{synch}} > 7 \times 10^{46}$ erg s⁻¹ since we do not include the high frequency side.

5. ELECTROMAGNETIC SIGNATURE OF THE ACCRETION FLOW

In this section, we explore the optical spectrum, near IR and mid IR photometry, in order to define the thermal emission of the accretion flow from the rest frame UV to the near IR (the signature of the quasar). There are two optical spectra of this quasar. The first observation was in 1985 with the Anglo-Australian Telescope (AAT, Dunlop et al. 1989). There is a 2003 March 23 Sloan Digital

Synchrotron Spectral Energy Distribution

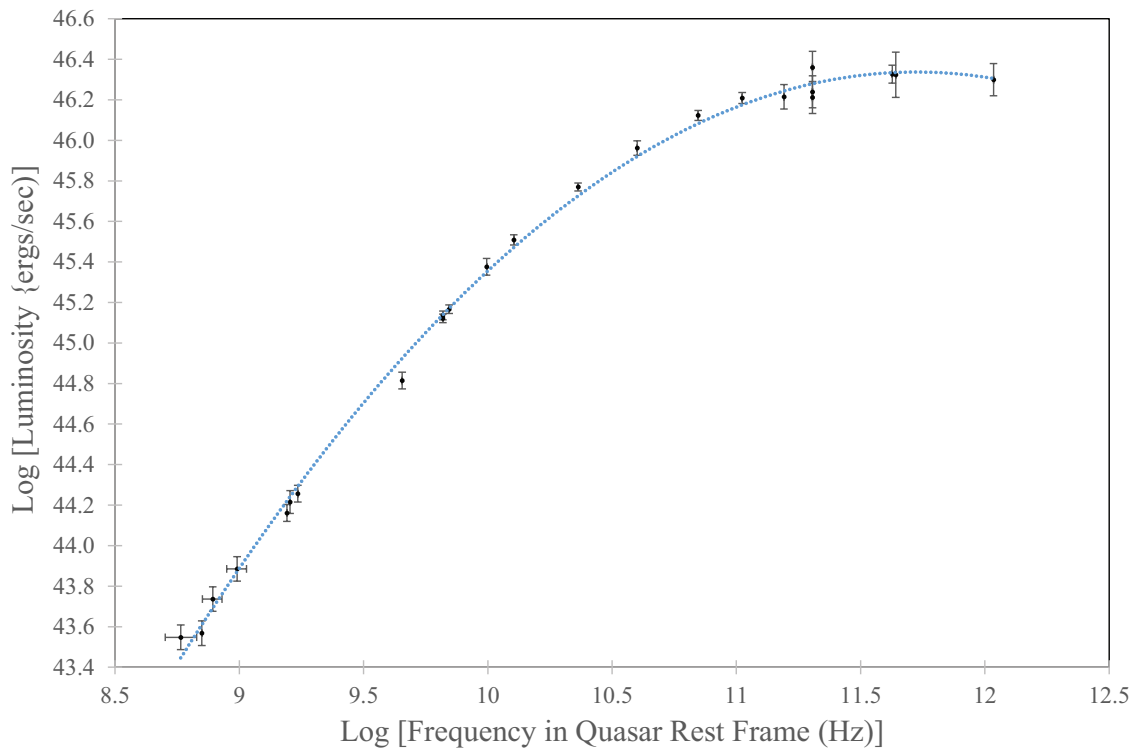


Figure 9. The synchrotron SED created from the data in Table 5. The luminosity of the low frequency portion of the SED (the plotted portion) has a luminosity of $\gtrsim 7 \times 10^{46} \text{ erg s}^{-1}$. The full synchrotron luminosity most certainly exceeds $10^{47} \text{ erg s}^{-1}$. The peak of the SED is $\nu_{\text{peak}} \approx 5 \times 10^{11} \text{ Hz}$ in the quasar rest frame.

Sky Survey (SDSS) spectrum that we show in the top frame of Figure 10. It has been corrected for Galactic extinction using the extinction values in the NASA Extragalactic Database (NED) applied to the models of Cardelli et al. (1989). There is very deep Ly α absorption from intervening gas short-ward of the Ly α emission from PKS 1351–018. The blue side of the Ly α broad emission line is completely truncated. The continuum spectral index defined in terms of the flux density as $F_\nu \propto \nu^{-\alpha_\nu}$ is $\alpha_\nu \approx 0.78$ long-ward of Ly α . This is typical of a radio quiet quasar. The *Hubble Space Telescope* (HST) composite spectral index was found to be $\alpha_\nu \approx 0.86$ (Zheng et al. 1997). Thus, this has a very strong accretion signature with very little influence of the jet synchrotron emission long-ward of Ly α (see IR discussion below). This means that there is no significant synchrotron dilution from the jet. Looking at the peak and turnover at $\approx 10^{12} \text{ Hz}$ in the synchrotron SED in Figure 10 and the SDSS SED in the bottom panel of Figure 10 this seems clear. The bottom panel of Figure 10 compares the SDSS data to the HST composite shape from Laor et al. (1997) and Zheng et al. (1997) to the spectrum in top panel after re-scaling to the continuum level of PKS 1351–018. We added photometry points from archival Mid-IR data in NED and IR observation found in the Data Release 11 of the United Kingdom Infrared Telescope (UKIRT) Deep Sky Survey⁷ (Lawrence et al. 2007).

⁷ <http://wsa.roe.ac.uk/index.html>

This shows the characteristic 1 micron dip in the quasar spectrum that appears in the composite. Thus, there is no evidence of synchrotron dilution even on the up-slope from the dip. Note the three photometry points from [Dunlop et al. \(1989\)](#). The B-band and R-band photometry lie right on top of the SDSS spectrum indicating very little variability between 1985 and 2003. The K-band data point in [Dunlop et al. \(1989\)](#) was taken with UKIRT, but disagrees with the value from the UKIRT Deep Sky Survey.

We can use the spectrum in [Figure 10](#) to estimate the bolometric thermal luminosity from the accretion flow, L_{bol} . The desired estimate does not include reprocessed radiation in the infrared from molecular clouds that are far from the active nucleus (not shown in the bottom panel of [Figure 10](#)). This would be double counting the thermal accretion emission that is reprocessed at mid-latitudes ([Davis and Laor 2011](#)). The most direct method is to use the UV continuum as a surrogate for L_{bol} . From the spectrum in [Figure 10](#) and the formula expressed in terms of quasar cosmological rest frame wavelength, λ_e , and spectral luminosity, L_{λ_e} , from [Punsly et al. \(2016\)](#),

$$L_{\text{bol}} \approx (4.0 \pm 0.7) \lambda_e L_{\lambda_e} (\lambda_e = 1350 \text{ \AA}) \approx (1.45 \pm 0.25) \times 10^{47} \text{ erg s}^{-1}. \quad (8)$$

The bolometric correction was estimated from a comparison to HST composite spectra of quasars with $L_{\text{bol}} \approx 10^{46} \text{ erg s}^{-1}$ ([Zheng et al. 1997](#); [Telfer et al. 2002](#); [Laor et al. 1997](#)).

Since Ly α is truncated by the Ly α forest, the only strong broad emission line (BEL) in the SDSS spectrum is C IV. In [Figure 11](#), we fit the C IV emission line into a common decomposition format, two broad lines and one narrow line ([Brotherton 1996](#); [Marziani et al. 2010](#); [Sulentic et al. 2000](#)). The blue (red) broad Gaussian component has a line center shifted $\approx 3900 \text{ km s}^{-1}$ ($\approx -390 \text{ km s}^{-1}$) with a FWHM of $\approx 3560 \text{ km s}^{-1}$ ($\approx 4860 \text{ km s}^{-1}$) and a luminosity of $\approx 9.3 \times 10^{43} \text{ erg s}^{-1}$ ($\approx 1.7 \times 10^{44} \text{ erg s}^{-1}$). The narrow line profile has a FWHM $\approx 1660 \text{ km s}^{-1}$ and a luminosity of $\approx 9.3 \times 10^{43} \text{ erg s}^{-1}$. There are two odd things about this line. First, it is a relatively weak broad line. The rest frame equivalent width (EW) is $\approx 13 \text{ \AA}$ and if we include the narrow line this only increases to $\text{EW} \approx 17 \text{ \AA}$. While the typical value from the HST sample of [Telfer et al. \(2002\)](#) is $\sim 60 \text{ \AA}$. As discussed earlier this is not a consequence of synchrotron dilution. We note that such small EWs are not unheard of as documented in [Baldwin et al. \(1989\)](#); [Diamond-Stanic et al. \(2009\)](#). The other odd feature is the strong blue excess which is typical of high luminosity radio quiet quasars, while quasars with powerful radio jets and lobes tend to have a red excess ([Richards et al 2002](#); [Punsly 2010](#)). The blue shifted Gaussian component is often considered evidence of a wind driven by the radiation pressure from the accretion flow ([Brotherton et al 1994](#); [Brotherton 1996](#); [Murray et al. 1995](#); [Netzer and Marziani 2010](#); [Sulentic et al. 2017](#)). This behavior seems to be explained by the large L_{bol} found in [Equation \(8\)](#). The quasar might have a high Eddington luminosity, but we have no reliable virial estimate in the absence of a broad low ionization line to measure.

6. γ -RAY BEHAVIOR

The ten year (from 2008 to 2018) average γ -ray luminosity detected by *Fermi*-LAT from 0.1 – 500 GeV (observed energy) is $L_{\gamma} = 5.78 \times 10^{47} \text{ erg s}^{-1}$ ([Sahakyan et al. 2020](#)). The temporal behavior of the γ -ray emission has been studied with low time resolution due to the low number statistics ([Li et al. 2018](#)). In this section, we explore higher time resolution in order to ascertain the peak γ -ray luminosity. The data reduction method is defined in ([Li et al. 2018](#)). In summary, the publicly *Fermi*-LAT Pass 8 data (P8R3_SOURCE_V2) and the *Fermitools* were used to perform the data analysis.

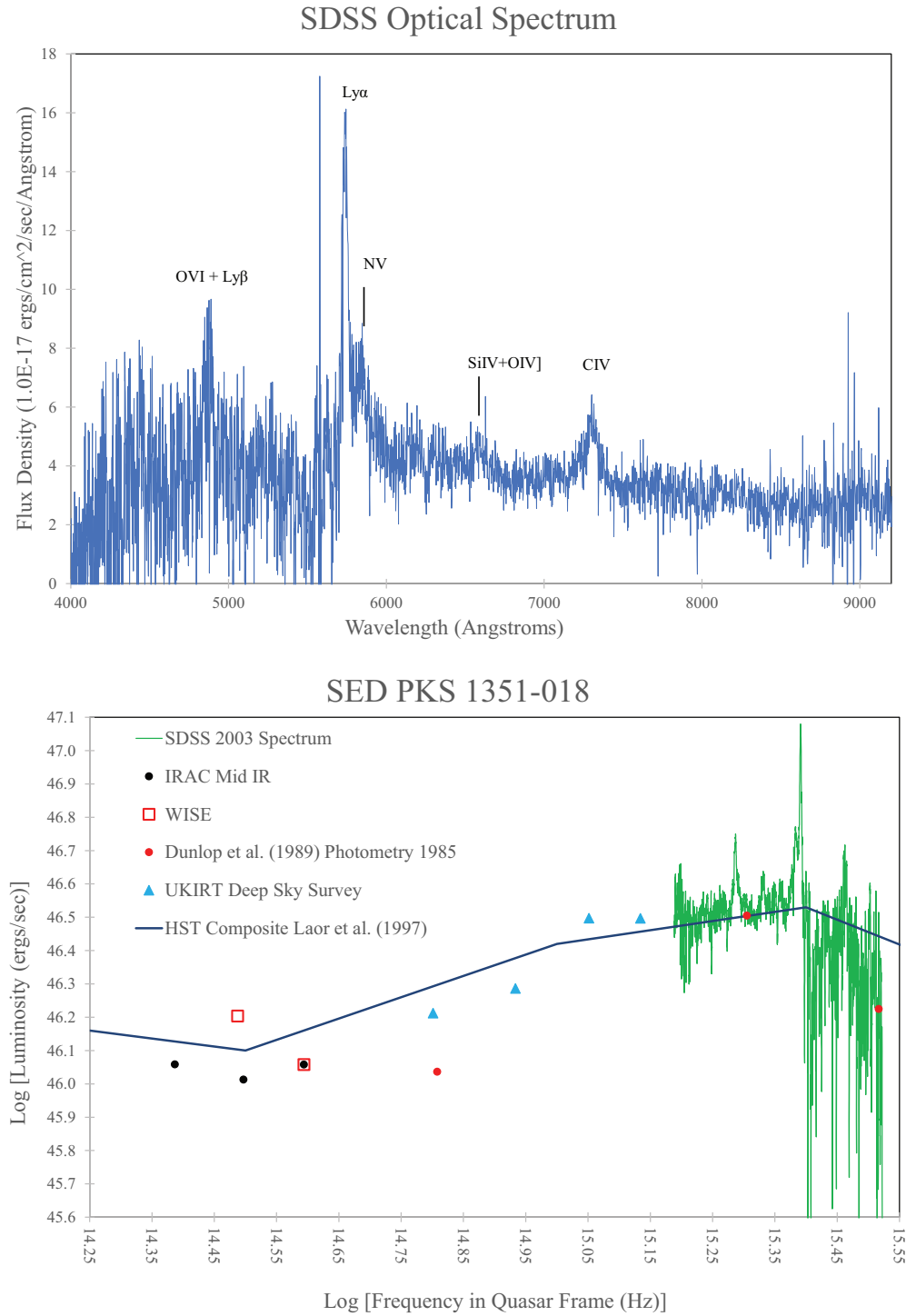


Figure 10. The top panel is the SDSS optical spectrum. There is strong Ly α absorption short-ward of the Ly α BEL. The prominent BELs are indicated. The bottom panel is the SED that includes some photometry points at different epochs. This is compared to the composite HST based spectrum (Laor et al. 1997; Telfer et al. 2002). The rest frame near IR to far UV SED is typical of a radio quiet spectrum. Optical and IR photometry at other epochs indicate very low variability compared to a blazar. This is consistent with the apparent turnover of the synchrotron SED at $\nu_{\text{peak}} \approx 5 \times 10^{11}$ Hz indicated in Figure 9.

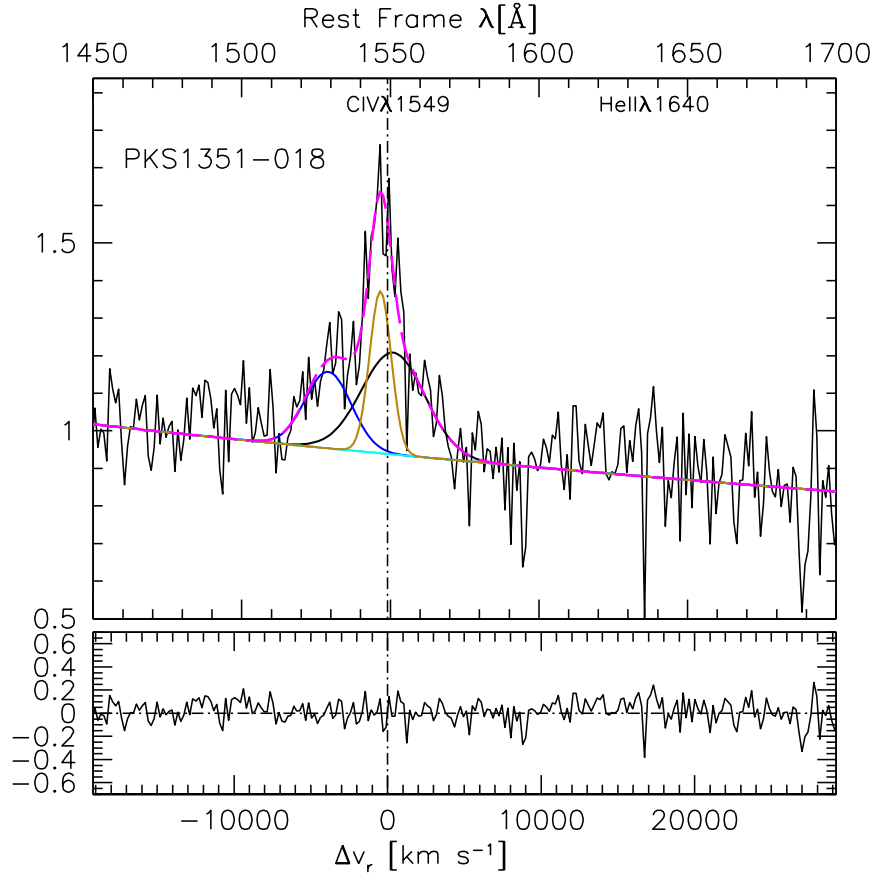


Figure 11. Even though the SDSS spectrum is noisy, it is of sufficient signal to noise to reveal the nature of the C IV emission line. The vertical axis is the flux density in the rest frame of the quasar in units of $3.7 \times 10^{-15} \text{ erg s}^{-1} \text{ cm}^{-2} \text{ \AA}^{-1}$, the continuum level at 1450 Å. The yellow Gaussian component is the narrow line emission. There are two broad components that were fit. The broader, more luminous of the two is slightly redshifted and is plotted in black. There is a highly blue-shifted Gaussian component plotted in blue. This is evidence of a strong, outwardly driven high ionization wind.

The data from 2008 August 4 to 2018 August 4 with the energy range from 100 MeV to 100 GeV was selected. We removed the γ -ray events with zenith angle greater than 90° and the quality-filter cuts (`DATA_QUAL==1` && `LAT_CONFIG==1`) are applied. We selected photons set within a 10° region of interest (ROI) and performed a unbinned likelihood analysis. The script `make4FGLxml.py`⁸ was used to generate the background model, which include all 4FGL-DR2⁹ sources within 15° around the target as well as `gll_iem_v07.fits` and `iso_P8R3_SOURCE_V2_v1.txt`. The spectra of the point sources within 10° around the center and the normalizations of the two diffuse emission backgrounds were set free. We determine the significance of the flare with the test statistic, TS (Mattox et al. 1996). The test statistic is defined as $\text{TS} = 2 \ln L/L_0$, where L and L_0 are the maximum likelihood values for the model with and without target source, respectively. The quantity TS was identified with a statistical significance of $\sqrt{\text{TS}} = n\sigma$ in Equation (22) and Figure 3 of Mattox et al. (1996).

⁸ <https://fermi.gsfc.nasa.gov/ssc/data/analysis/user/make4FGLxml.py>

⁹ https://fermi.gsfc.nasa.gov/ssc/data/access/lat/10yr_catalog/

We consider two likely flares in 2011 and 2016 that were previously identified with ~ 5 month time sampling (Li et al. 2018). Since we already know that the flare is present, Figure 12 considers higher time resolution of the *Fermi*-LAT light curves at these epochs. We consider 3 week bins or 4.5 days in the quasar rest frame.

The vertical axis in Figure 12 is the 0.1 – 100 GeV luminosity. The first flare seems more prolonged, but the second flare was brighter. The peak flare luminosity was $\approx 6 \times 10^{48}$ erg s $^{-1}$. With finer sampling (3 days), this increases to $\approx 10^{49}$ erg s $^{-1}$, but TS falls below 25, TS $\gtrsim 20$. The SED in the γ -ray region is very steeply decreasing power law ($\alpha \approx 2$) as expected for strong external inverse Compton cooling from the existence of the luminous quasar environment that was described in the last section (Sahakyan et al. 2020; Marcotulli et al. 2020). This combined with the high redshift indicates that most of the γ -ray luminosity is most likely at observed energies < 0.1 GeV. Thus, it is quite possible that the 2016 γ -ray flare is of comparable luminosity to some of the strongest known γ -ray flares (Abdo et al. 2011).

7. SYNCHROTRON SELF ABSORBED POWER LAW FIT TO THE RADIO DATA

A synchrotron self absorbed power law (SSA power law) for the observed flux density, S_{ν_o} , is the solution to the radiative transfer in a homogeneous medium such as a uniform spherical volume (Ginzburg and Syrovatskii 1965; van der Laan 1966):

$$S_{\nu_o} = \frac{S_o \nu_o^{-\alpha}}{\tau(\nu_o)} \times (1 - e^{-\tau(\nu_o)}) \quad , \quad \tau(\nu_o) = \bar{\tau} \nu_o^{(-2.5+\alpha)} \quad , \quad (9)$$

where $\tau(\nu)$ is the SSA opacity, S_o is a normalization factor and $\bar{\tau}$ is a constant. The wide spectral peak requires three SSA power law components. Adding a fourth SSA power law does not improve the fit. In Figure 13, we show the three components of the SSA power law fit that are naturally associated with the un-resolved nucleus, the Southeast Component and the North Lobe. The power laws for the core, Southeast Component and North Lobe are approximated by the data from $\nu_o = 5$ GHz to $\nu_o = 22$ GHz in Table 5, Figure 8, and the VLBI data in Tables 1, 3 and 4, respectively. Fine adjustment of the SSA power law parameters proceeds until the residuals (see Equation (3)) of the fit to the total flux density from $\nu_o = 120$ MHz to $\nu_o = 22$ GHz are minimized. The fit is based on two important assumptions that are motivated by the observations in Tables 1, 3 and 4 that are described below.

7.1. Assumption 1: VLBI Does Not Capture All of the North Lobe Flux at High Frequency

Since the North Lobe is a diffuse, steep spectrum, component, there will be a tendency for VLBI to resolve out some of the diffuse emission due to limited dynamic range associated with imperfect (u, v) coverage. This effect is most pronounced at high frequency due to the lower flux density. This is clearly evident in the deep VLBA image at 15.4 GHz in Table 4 that does not detect the North Lobe, even though we expected at least 6.5 mJy to be present. Other evidence of this is the 2000 Jun 05 C-band observation in Table 3. This is the longest VLBI (which includes the VLBA baselines) observation (best (u, v) coverage) and it detects the largest flux density of the North Lobe of any C-band observation. To compensate for this effect, the fit to the North Lobe flux is biased towards the top of the error bars at high frequency. This is a valid compensatory device if the observations are sufficiently sensitive (i.e., large fractions of the flux are not resolved out). Thus, the three long duration C-band VLBI observations before 2014 in Table 3 are used in the fit to Figure 13 and the

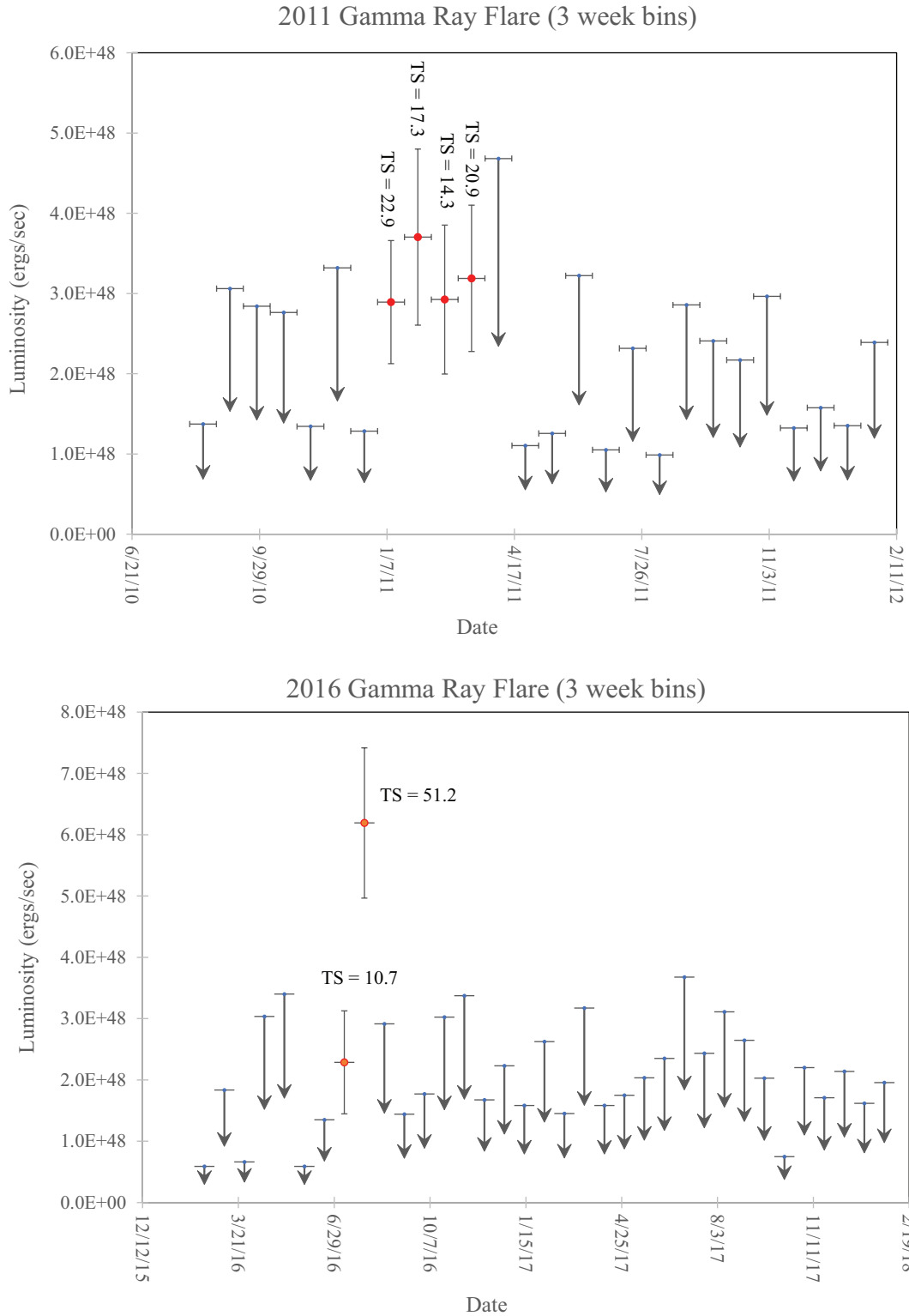


Figure 12. The top panel is the light curve of the 2011 flare sampled in 3 week bins. It is detected in a few consecutive bins but with, $TS < 25$. This suggests a prolonged faint flare. The vertical axis is the 0.1 – 100 GeV luminosity. The 2016 flare is plotted similarly in the bottom panel.

observations with short scans and poor (u,v) coverage from 2014 onward are ignored. A direct fit to the data without this biasing towards the top of the error bars yields a power law with $\alpha = 0.85$. We consider the bias towards the tops of the high frequency error bars in Figure 13, which yields $\alpha = 0.75$, to be a more plausible reconstruction of the physical source of lobe emission that is consistent with the observed data.

7.2. Assumption 2: The Knot in the North Jet is Negligible to the Fit

The Knot in the North Jet that appears in Table 3 is not considered as an important contributor to the total flux density at any frequency for the following reasons.

1. The knot in the north jet is only detected at C-band. Thus, there is no spectral data and therefore no basis to extrapolate this to other frequencies.
2. According to Table 3, the feature is not detected at C-band in 1995 Jan 28 and only has 4 mJy in the full track VLBA observation in 2001 Jan 23.
3. The feature seems to move from 1.6 mas to ~ 5.5 mas when it is detected in Table 3 and might not be the same feature.
4. At C-band, it is much weaker than the nucleus and does not affect the fit in this region. The fit to the total flux density is determined by the core spectrum at all frequencies above C-band.
5. The Knot in the North Jet is at least one order of magnitude smaller than the North Lobe in Table 3. Being so compact, it is likely that the low frequency spectral turnover is at much higher frequency than the North Lobe (van der Laan 1966; Moffet 1975; Ezeugo and Ubachukwu 2010). Thus, the knot likely contributes insignificantly at frequencies below 350 MHz compared to the North Lobe (where the North Lobe is prominent).
6. As noted above, a fourth SSA power law does not improve the fit to the total flux density.

8. A PHYSICAL MODEL OF THE NORTH LOBE SSA POWER LAW

Once an SSA power law is chosen for the North Lobe, we are interested in a physical model that is responsible. Complicated dynamics are most likely occurring in the radio lobe (Blundell and Rawlings 2000). In general, there are fine-scale features such as shock fronts and filaments embedded within the diffuse lobe plasma. However, our image in Figure 3 is a structure-less plume that we fit as a circular Gaussian. There is no observational evidence to justify a model more complicated than a homogeneous, spherical, single zone of plasma. Single zone spherical models are a standard technique even in blazar jet calculations out of practical necessity including previous treatments of this source (Ghisellini et al. 2010; Sahakyan et al. 2020; Marcotulli et al. 2020). A simple homogeneous spherical volume model or plasmoid has historically provided an understanding of the spectra and the time evolution of astrophysical radio sources (van der Laan 1966). We have used this formalism to study a panoply of phenomena, major flares in a Galactic black hole, a γ -ray burst and flares in a radio quiet quasar (Punsly 2012, 2019; Reynolds et al. 2009, 2020). Most importantly, we used this method in Punsly et al. (2020) to study the radio lobes in the super-luminous radio quasar, 3C 82 (which should be consulted for the details of the calculational method). The SSA turnover provides information on the size of the region that produces the preponderance of emission. This can be tied directly to

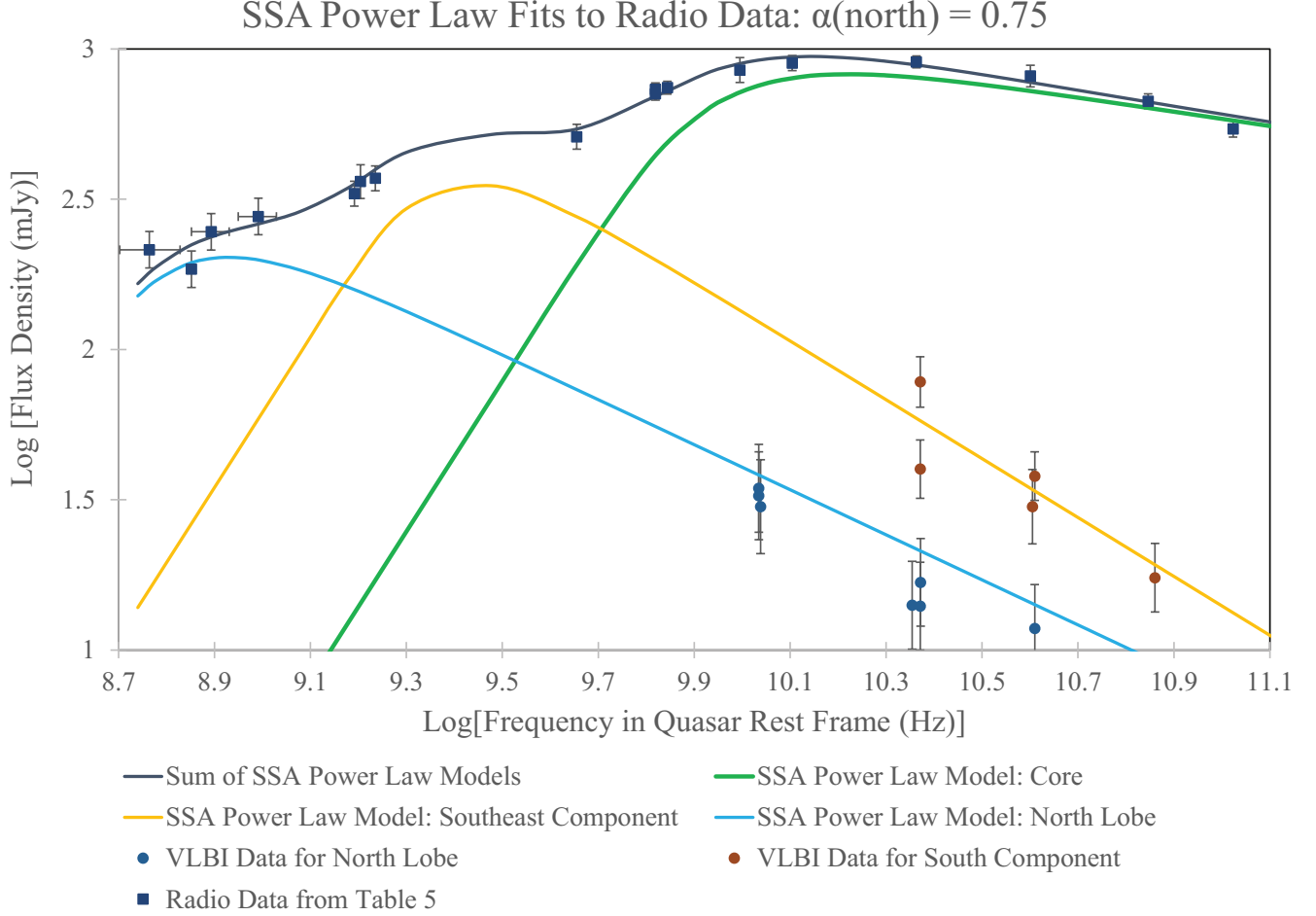


Figure 13. The figure shows the best fit of the three component SSA power law model to the total flux density of PKS 1351–018. A realistic fit to the North Lobe should be biased toward the top of the high frequency error bars for this diffuse structure due to the limited dynamic range of these VLBI data.

the image in Figure 3. Furthermore, these models do not need to invoke equipartition in order to produce a solution.

We have established three physical constraints. Firstly, the FWHM of the North Lobe of the 2002 S-band observation (the best depiction of the lobe) in Table 1 constrains the sphere radius, R ,

$$R \approx 3.3 \text{ mas} . \quad (10)$$

Secondly, the apparent velocity, v_{app} , is bounded by 23 years of C-band radio images as indicated in Figure 6,

$$v_{\text{app}} < 0.57 c . \quad (11)$$

Thirdly, the light curve variability analysis of the flare in Figure 2 and Equation (6) provide an approximate constraint on the line of sight to the jet axis, θ ,

$$\theta < \theta_{\text{max}} \sim 10^\circ . \quad (12)$$

Note that this constraint is looser than Equation (6) because that derivation assumed no uncertainty arising from the fitting technique in Figure 2. Equations (11) and (12) combine to give a constraint on δ . From Rees (1966) and Ginzburg and Syrovatskii (1969),

$$\beta_{\text{app}} \equiv \frac{v_{\text{app}}}{c} = \frac{\beta \sin \theta}{1 - \beta \cos \theta}, \quad (13)$$

where β is the three-velocity of the moving plasmoid. Combining the definition of the Doppler factor, $\delta = \sqrt{1 - \beta^2} / (1 - \beta \cos \theta)$, with Equations (11) and (12) yields an equivalence to a constraint on the Doppler factor in our models. This can be emphasized by writing the Doppler factor as $\delta(\beta_{\text{app}}, \theta)$.

The value of minimum lepton energy, E_{min} , is not constrained directly by observation. Values of $E_{\text{min}} = m_e c^2$ and $E_{\text{min}} = 2.6 m_e c^2$ are used in Marcotulli et al. (2020) and Sahakyan et al. (2020), respectively, to fit the synchrotron peak and the inverse Compton spectrum from the nucleus. Here m_e denotes the electron mass. Since this is the region with the most energetic electrons, we do not expect E_{min} to be larger in the less energetic North Lobe. We also note that Celotti and Ghisellini (2008) have argued that $E_{\text{min}} = m_e c^2$ based on fits to blazar jet spectra in the soft X-ray band. Thus, we initially consider $E_{\text{min}} = m_e c^2$ and explore slightly higher values later. There is not a unique solution to the physical parameters of the North Lobe that recreate the fit in Figure 13. In this section we explore the solution space as calculated in (Punsly et al. 2020).

8.1. Kinematics of the Lobe Solution

We separate the energy content of the turbulent magnetized lobe into two pieces. The first is the kinetic energy of the protons, $\mathcal{K}(\text{protonic})$,

$$\mathcal{K}(\text{protonic}) = (\gamma - 1) M c^2, \quad (14)$$

where M is the mass of the plasmoid and γ is the Lorentz factor in the quasar rest frame. The other component is the lepto-magnetic energy, $E(\text{lm})$, the volume integral of the leptonic internal energy density, U_e , and the magnetic field energy density, U_B . In a spherical volume,

$$E(\text{lm}) = \int (U_B + U_e) dV = \frac{4}{3} \pi R^3 \left[\frac{B^2}{8\pi} + \int_{\Gamma_{\text{min}}}^{\Gamma_{\text{max}}} (m_e c^2) (N_{\Gamma} E^{-n+1}) dE \right], \quad (15)$$

where in the proper frame, B is the magnetic field, N_{Γ} is the normalization of the number density power law and $\Gamma(m_e c^2)$ is the lepton energy. The corresponding energy density is $U(\text{lm}) \equiv U_e + U_B$. The leptons also have a kinetic energy analogous to Equation (14),

$$\mathcal{K}(\text{leptonic}) = (\gamma - 1) \mathcal{N}_e m_e c^2, \quad (16)$$

where \mathcal{N}_e is the total number of leptons in the lobe.

There are protonic and leptonic energy fluxes due to bulk motion. The protonic energy flux is approximately the kinetic energy flux,

$$\mathcal{E}(\text{proton}) = N(\gamma - 1) \gamma v_{\text{adv}} m_p c^2, \quad (17)$$

where m_p is the mass of the proton, N is the proper number density, and v_{adv} is the advance speed of the lobe in the quasar rest frame. The magneto-leptonic energy flux is

$$\mathcal{K}(\text{magneto-leptonic}) = N \gamma v_{\text{adv}} [\gamma \mu c^2], \quad (18)$$

where μ is the specific enthalpy (Punsly 2008). The specific enthalpy decomposes as

$$N\mu = U(\text{lm}) + P, \quad (19)$$

where the relativistic pressure, $P \approx (1/3)U(\text{lm})$ (Willott et al. 1999).

With the leptonic assumption, Equation (18) implies that the kinetic luminosity (jet power), Q_{lm} , is

$$Q_{\text{lm}} = \int [\mathcal{K}(\text{magneto} - \text{leptonic})] dA_{\perp} + L_{\text{r}}, \quad (20)$$

where dA_{\perp} is the cross sectional area element normal to the jet axis and L_{r} is the energy flux lost to radiation. .

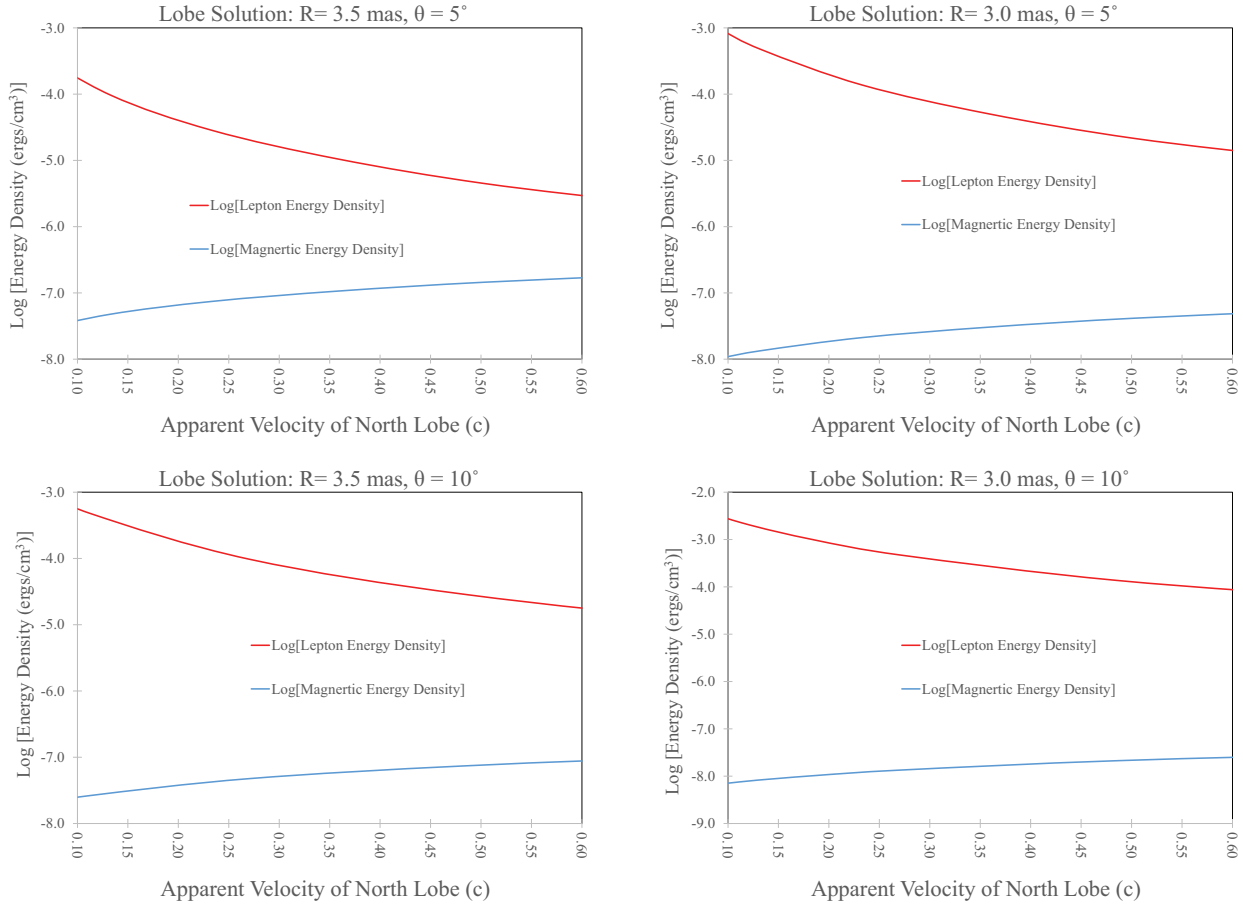


Figure 14. This figure explores a large subset of the solution space for a spherical plasmoid that radiates the fit to the North Lobe Figure 13. Based on Equations (10) and (12), we choose a rectangular subset $3.0 \text{ mas} < R < 3.5 \text{ mas}$ and $5^\circ < \theta < 10^\circ$ and bound its behavior by looking at the four corners of the rectangle. By plotting U_e and U_B as a function of β_{app} , we find no solutions that are near equipartition and obey the upper bound on β_{app} from Equation (11). The closest solution to equipartition is at $R = 3.5 \text{ mas}$ and $\theta = 5^\circ$ in the upper left hand panel.

The first thing that we noticed about the infinite set of solutions that conform to Equations (10)–(12) is that most of this domain yields solutions that are extremely inertially dominated, $U_e \gg U_B$.

The results are plotted in Figure 14 for the four corners of the rectangular domain of the two dimensional set of pre-assigned values of $3.0 \text{ mas} < R < 3.5 \text{ mas}$ and $5^\circ < \theta < 10^\circ$. There is no solution near equipartition with the constraint of Equation (11) imposed, $\beta_{\text{app}} < 0.57$.

These extremely inertially dominated solutions are disfavored on both theoretical and empirical grounds. Theoretically, the pair plasma is highly energetic with large random velocities, and one would expect a relatively strong tangled magnetic field to form. Empirically, the radio lobes of powerful Fanaroff–Riley II (FR II) radio galaxies have magnetic fields that tend to be near equipartition or slightly below this (Fanaroff and Riley 1974; Ineson et al. 2017; Kataoka and Stawarz 2005). A large sample of FR II radio galaxy lobes was studied in X-rays and with multi-frequency radio imaging (Ineson et al. 2017). The X-ray observations were used to determine the inverse Compton emission (primarily of the Cosmic Microwave Background) and the radio images were used to determine the synchrotron emission. From this they were able to estimate U_e/U_B . In Figure 2 of Ineson et al. (2017), they found, $E_{\text{equipartition}} < E(\text{lm}) < 7E_{\text{equipartition}}$, in the pair plasma of the lobes, where $E_{\text{equipartition}}$ is the equipartition lepto-magnetic energy. The median value is $E(\text{lm}) \approx 2.4E_{\text{equipartition}}$. We consider this range of possible values for the North Lobe of PKS 1351–018 in the following analysis. In order for this to be robust, we comment on our description of the northern component as a lobe. Recall that the MERLIN observation with a resolution $\sim 50 - 60 \text{ mas}$ could not detect anything, except for a point source. The VLBI S-band image in Figure 3 did not detect anything farther from the nucleus (within $\sim 30 \text{ mas}$ of the nucleus) than the North Lobe. The results of Table 2 indicate that the better S-band VLBI observations are consistent with minimal or no missing flux density in the image. The North Lobe is therefore likely to be the furthest emission region from the nucleus. It appears to be at the end of a curving continuous jet in Figure 4. Based on the Gaussian fit in Tables 1 and 3, it is definitely wider than the jet, indicating a difference in the physical composition. One could claim that it is a knot in a continuous jet that appears to be at its terminus. This would mean that it is predominantly the hot spot in the lobe that is detected. There does not seem to be edge brightening in Figures 3 and 4 that is characteristic of the hot spot in FR II radio lobes (Fanaroff and Riley 1974). However, the lack of edge brightening could be an artifact of the imperfect (u, v) coverage and insufficient resolution. We do not think this to be the case since the North Lobe seems to be significantly inflated relative to the jet. In any event, our jet analysis does not depend on this distinction. The hot spots in FR II radio lobes and the lobe plasma deviate similarly from equipartition. The hot spots have been found to have internal energies relative to equipartition in a range very similar to the lobes (Kataoka and Stawarz 2005).

Figure 14 indicates that the larger value of R and the smaller value of θ moves the solutions closer to equipartition. Thus motivated, we look at the $R = 3.5 \text{ mas}$ case with $\theta < 5^\circ$ as a possible viable region of the solution space. The first thing that we explore is the dependence of U_e and U_B on δ in the top left hand panel of Figure 15. It is clear that for $E_{\text{equipartition}} < E(\text{lm}) < 7E_{\text{equipartition}}$, $\delta \lesssim 5.5$. This is a large Doppler factor for the modest apparent velocity in Equation (11). This is explained with Equation (13) as a consequence of a small LOS.

The top right hand panel of Figure 15 plots β_{app} as a function of the angle to the LOS under four different constraints, in the range $E_{\text{equipartition}} < E(\text{lm}) < 7E_{\text{equipartition}}$. As U_B/U_e is lowered, a larger LOS is consistent with $\beta_{\text{app}} < 0.57$. Even so, the largest LOS angle in any of the plausible models is $\approx 5.8^\circ$ for $E(\text{lm}) = 7E_{\text{equipartition}}$. The bottom left hand panel uses Equation (20) to plot the lepto-magnetic jet power, Q_{lm} , as a function of the LOS angle for four cases in the range,

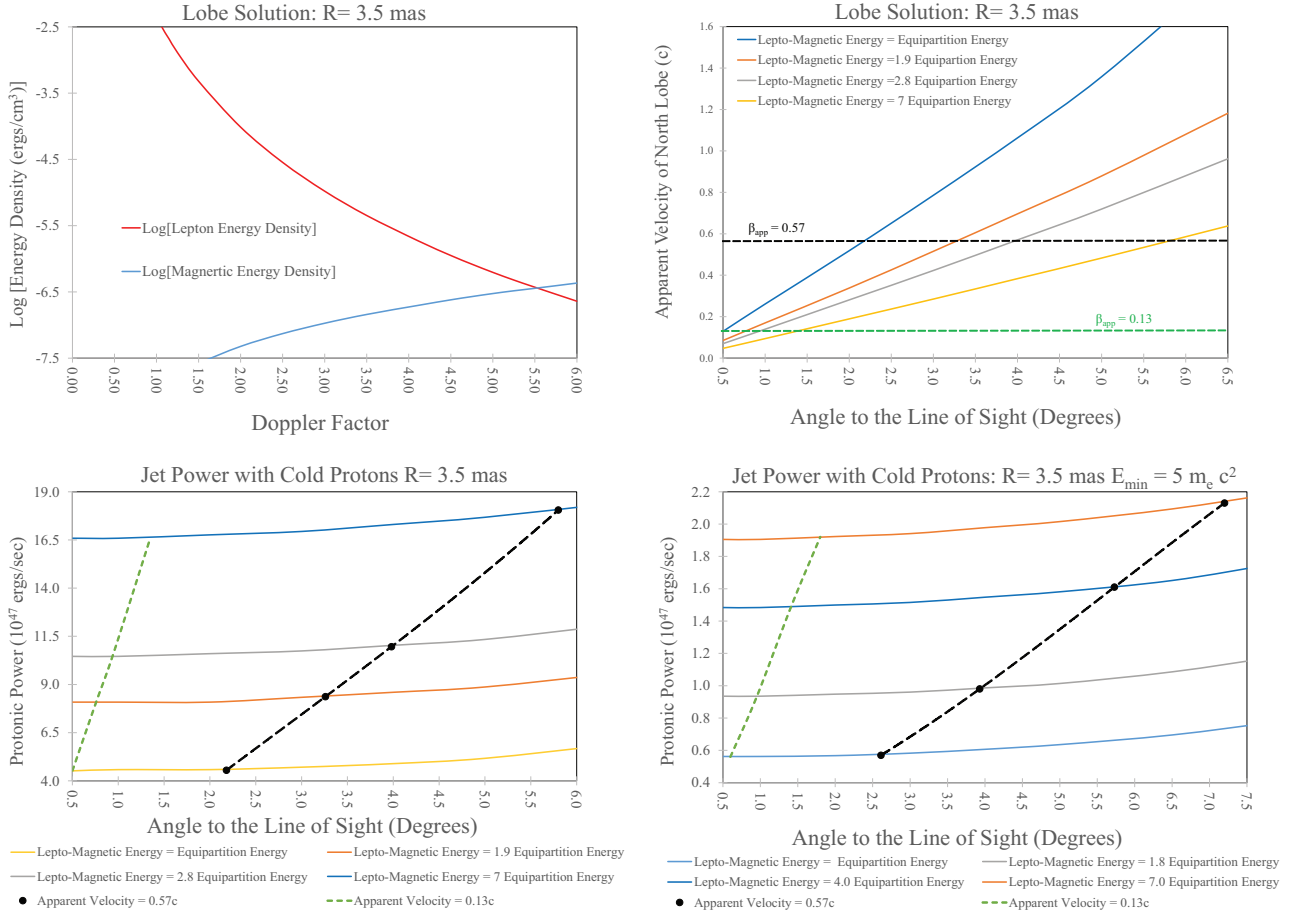


Figure 15. The figure presents plots that describe the properties of the preferred solution for the lepton-positron lobe model. The top left hand panel shows the connection between the energy density of the magnetic field and the energy density of the leptons as a function of δ . Ostensibly, the plot appears to be independent of β_{app} and θ . However, as discussed earlier, that dependency is contained within the dependent variable, $\delta(\beta_{app}, \theta)$. The top right hand panel shows how β_{app} depends on θ for four families of solutions with energy densities consistent with the FR II energy densities found in FR II radio lobes [Ineson et al. \(2017\)](#). The bottom left hand frame is the estimated power of the lepto-magnetic jet feeding the lobes as a function of the LOS for these same four families of solutions. Note the dashed black curve that represents the upper limit from Figure 6 of $\beta_{app} < 0.57$. The only solutions consistent with this observational constraint are to the left of the dashed curve. The green dashed curve are solutions with the best fit velocity from Figure 6. The bottom right hand panel is a similar plot with the condition $E_{min} = 5m_e c^2$ instead of $E_{min} = m_e c^2$ as was assumed in the other three panels. The change in the estimated jet power is $\approx 35\%$.

$E_{equipatition} < E(lm) < 7E_{equipatition}$. The black dashed curve represents the $\beta_{app} = 0.57$ upper limit implied by Figure 6. The only solutions consistent with observation are to the left of the black dashed curve. We also investigate the consequences of abandoning the $E_{min} = m_e c^2$ assumption. The bottom right hand panel is a plot of Q_{lm} as a function of the LOS angle, assuming that $E_{min} = 5m_e c^2$. This value is motivated by the model of the γ -ray emission in [Sahakyan et al. \(2020\)](#) which has $E_{min} = 2.6m_e c^2$ in the nucleus. We intentionally went above this value in order to bound a range of plausible assumptions. However it is not clear why E_{min} would exceed $m_e c^2$ and is included for

the sake of completeness. There is only modest variation over the entire plausible parameter range $Q_{\text{lm}} \approx (5.2 \pm 3.2) \times 10^{45} \text{ erg s}^{-1}$. Note that the allowed LOS angle increases to 7.2° when $E_{\text{min}} = 5m_e c^2$. The core synchrotron and inverse Compton emission (γ -ray emission) was used in Sahakyan et al. (2020) and Marcotulli et al. (2020) to estimate $Q_{\text{lm}} = 2.76 \times 10^{45} \text{ erg s}^{-1}$ and $Q_{\text{lm}} = 4.24 \times 10^{45} \text{ erg s}^{-1}$, respectively. Remarkably, the lepto-magnetic jet power estimates on sub-parsec scales agree with our estimate $\sim 2.5 \text{ kpc}$ (after de-projection) farther out in the North Lobe. If there is a (Doppler deboosted) counter-jet, the total power of the central engine would be $Q_{\text{lm}} \approx (1.04 \pm 0.64) \times 10^{46} \text{ erg s}^{-1}$.

We validate that the energy budget in the approaching jet derived from the North Lobe is sufficient to support the radiation losses. The intrinsic γ -ray luminosity, $L_\gamma(\text{intrinsic}) = \delta^{-4} L_\gamma(\text{apparent})$. From the estimated δ in the γ -ray emitting region from Sahakyan et al. (2020) and the value of δ from Marcotulli et al. (2020), we find $L_\gamma(\text{intrinsic}) = (20.47^{-4}) 5.78 \times 10^{47} \text{ erg s}^{-1} = 3.29 \times 10^{42} \text{ erg s}^{-1}$ and $L_\gamma(\text{intrinsic}) = (15.4^{-4}) 5.78 \times 10^{47} \text{ erg s}^{-1} = 1.03 \times 10^{43} \text{ erg s}^{-1}$, respectively for the time averaged $L_\gamma(\text{apparent})$ from Section 6. Even if we look at the peak flare luminosity in 2016 in a 3 week bin in Figure 12, this only increases by an order of magnitude. The energy budget of the jet that is dissipated as γ -rays and the synchrotron peak is a negligible fraction of the total jet power.

We can also estimate the $P\Delta V$ work of inflating the lobe in the environment of the host galaxy. From Figure 2 of Mathews and Brighenti (2003), we get an estimate of an external pressure on the order of 1 kpc from the nucleus (where most of the lobe propagation occurs), $P_{\text{ext}} \sim 10^{-10} \text{ dyn cm}^{-2}$ if the host galaxy is a large elliptical. From the expression for the pressure, below Equation (19), the internal lobe pressures are $2 \times 10^{-7} \text{ dyn cm}^{-2} < P < 2 \times 10^{-6} \text{ dyn cm}^{-2}$ for the solutions in Figure 15. The North Lobe is highly over-pressurized relative to the environment. Much more jet energy is required to energize the plasma in the lobe volume than is required to push the enveloping gas away as this volume inflates. We conclude that the $P\Delta V$ work of inflating the lobe is insignificant in our jet power estimates.

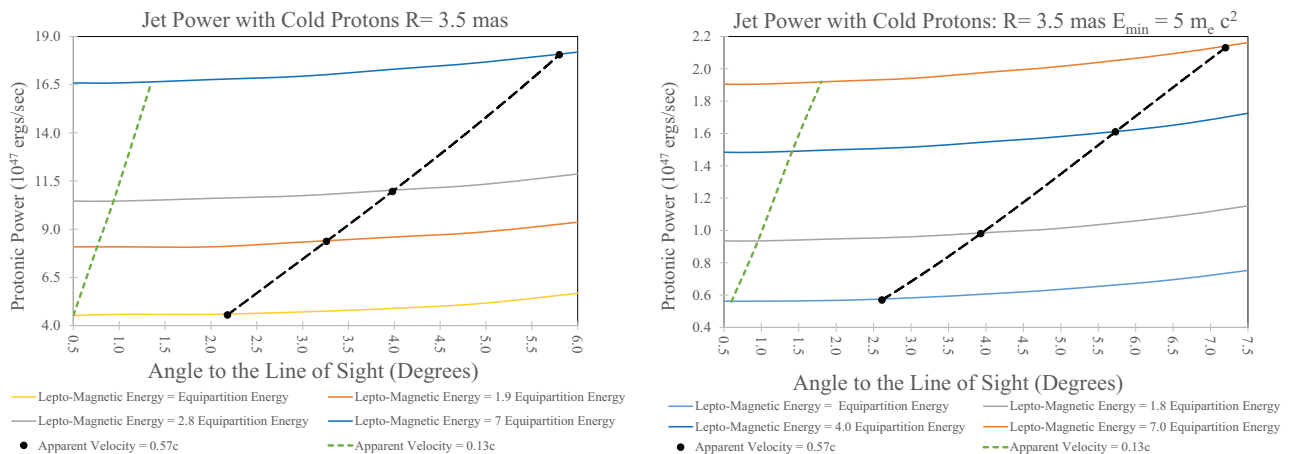


Figure 16. The jet power computed under the assumption that the positive charges are cold protons. Otherwise, the plots are identical in format to the bottom two panels of Figure 15. The allowable physical solutions exist to the left of the black dashed curves. The green dashed curve represents solutions with the apparent velocity derived from the fit to the component separation in Figure 6.

8.2. A Protonic North Lobe

In principle, the positive charges in the ionized lobes can be protonic matter instead of positronic matter. This was proposed by [Marcotulli et al. \(2020\)](#) in their model of the γ -ray emitting region. These are not thermal protons that add to the pressure, but cold protons. A significant thermal proton population in FR II radio lobes has been argued to be implausible ([Croston et al. 2018](#)). Based on Equations (16) and (18), the kinetic energy of the protons would be much larger than $E(\text{lm})$. The spectrum is created by electrons that radiate in the magnetic field. The spectrum is still depicted by the fit in Figure 13. However, the kinetic luminosity of the moving lobe computed from Equation (17) is much larger in Figure 16 compared to the bottom panels of Figure 15. We find no compelling reason to add these cold protons, but we cannot prove that this is not the case. One thing that is not encouraging is the kinetic luminosity of the protons in the lobe is an order of magnitude larger than [Marcotulli et al. \(2020\)](#) estimated in the γ -ray region.

9. DISCUSSION AND CONCLUDING REMARKS

The quasar, PKS 1351–018, is at the high end of the quasar synchrotron luminosity distribution, $> 10^{47}$ ergs/sec (Section 4). The synchrotron spectrum displays very benign blazar characteristics. In particular, the radio flux density is mildly variable even at 100 GHz in the quasar rest frame. But to the contrary, there were two strong γ -ray flares in 2011 and 2016 as shown in Section 6. We explore this dichotomous behavior through various analyses in this paper. In Section 2, the $\nu_o = 5$ GHz ($\nu = 23.5$ GHz) light curve was created. Even though the variability tends to be on the same order of magnitude as the measurement uncertainty, we were able to find a flaring event in 1990 that required a relativistic outflow with a LOS $< 7.1^\circ$ to the jet. In Section 3, we studied the VLBI images at various frequencies from 1995 to 2020. Combined with VLA and MERLIN images, we determine that the source is very compact, confined within ~ 15 mas. There is a conspicuous lobe-like feature to the north at the end of a jet 12 mas from the nucleus. It appears very steady in both position and flux density over 23 years. We use these properties to constrain a physical model of the lobe in Sections 7 and 8. The kinematics of the lobe are used to estimate the jet power, $Q \approx (5.2 \pm 3.2) \times 10^{45}$ erg s $^{-1}$, with quite possibly a similar energy flux directed in a counter jet. The physical model is corroborated by two independent results. The jet power agrees with the jet power estimated from studies of the γ -ray flares in the nucleus ($\sim 1 - 3$ kpc away) based on completely different assumptions and physical conditions. Furthermore, a polar LOS $< 5.8^\circ$ is required for any realistic physical model of the North Lobe, a derivation that is independent of the light curve analysis in Section 2.

We also note that there might be an interaction between the jet and the high ionization wind indicated from the spectral analysis in Section 5. The jet is very highly curved based on Tables 1, 3 and 4, even compared to most blazars ([Britzen et al. 2008](#); [Kharb et al. 2010](#)). The curving jet is most clearly illustrated in the right hand panel of Figure 5. Based on the elongation of the nuclear Gaussian in multiple epochs the jet begins in the southwest direction in the first 0.5 – 0.7 mas, then it swings to the southeast at about 1.1 mas from the nucleus. Apparently, after passing through the “knot in the north jet” about 2 – 3 mas from the nucleus in the northeast quadrant, it ends up slightly west of north in the North Lobe. The jet direction rotates $\sim 210^\circ$. Most likely, the bending is enhanced by Doppler aberration, but this does not preclude some modest intrinsic bending. In fact there needs to be some intrinsic or seed bending that is magnified by Doppler aberration. The shear layer between the jet and the denser, slower wind can decelerate the jet and possibly deflect the trajectory a few degrees. This could reduce the magnitude of the relativistic effects, thereby

stabilizing the synchrotron luminosity and explain the large swing in the jet PA. This is speculative, but it does tie together three, otherwise coincidental, extreme behaviors of the source:

- A luminous high ionization wind moving at $\sim 4000 \text{ km s}^{-1}$ is rare in radio loud quasars (Punsly 2010; Richards et al 2002). Such a fast wind is rare even for luminous radio quiet quasars (Sulentic et al. 2017).
- The parsec scale jet trajectory bends 210° .
- The preponderance of the enormous synchrotron flux is emitted by a region that has low variability.

10. ACKNOWLEDGMENTS

We are grateful to the referee who had many useful comments that improved this work. Matt Lister provided many VLBI fits that benefitted the early stages of this work and motivated the path going forward. We are grateful to Lorant Sjouwerman, Jamie Stevens, and Natasha Hurley-Walker for help and guidance with the NVAS, ATCA and GLEAM data, respectively. Marco Berton and Matt Stevens generously provided useful JVLA data reductions. We thank Shane O’Sullivan for the 5 GHz VLBI images and fits. We were also fortunate to be helped by Narek Sahakyan, Lea Marcotulli and Vaidehi Paliya with the high energy data. Wendy Peters generously provided us with VLITE data. Basic research in radio astronomy at the U.S. Naval Research Laboratory is supported by 6.1 Base Funding. Construction and installation of VLITE was supported by the NRL Sustainment Restoration and Maintenance fund. The VLA is operated by the National Radio Astronomy Observatory (NRAO). We would like to thank Anita Richards of the MERLIN/VLBI National Facility for supplying the 5 GHz data. This work was supported by the National Radio Astronomy Observatory, a facility of the National Science Foundation operated under cooperative agreement by Associated Universities, Inc. This publication made use of the Astrogeo VLBI FITS image database ([http://astrogeo.org/vlbi/\\$images/](http://astrogeo.org/vlbi/$images/)) maintained by Leonid Petrov. SF thanks the Hungarian National Research, Development and Innovation Office (OTKA K134213) for support. ABP was supported by the Russian Science Foundation grant 21-12-00241.

REFERENCES

- | | |
|--|---|
| Abdo, A. A., Ackermann, M., Ajello, M., et al. 2011, ApJL, 733, L26 | Brotherton, M., Wills B., Steidel, C., Sargent, W. 1994, ApJ, 430, 131 |
| Ackermann, M., Ajello, M., Baldini, L., et al. 2017, ApJL, 837, L5 | Brotherton, M. 1996, ApJS, 102, 1 |
| Baldwin., J., Wampler, E., Gaskell, M. 1989, ApJ, 338, 630 | Cardelli, J., Clayton, G., Mathis, J. 1989, ApJ, 345, 245 |
| Becker., R., White, R. L., Helfand D. 1995, ApJ, 450, 595 | Celotti, A., and Ghisellini, G. 2008, MNRAS, 385, 283 |
| Bicknell, G., de Ruiter, H., Fanti, R., Morganti, R., Parma, P. 1990, ApJ, 354, 98 | Clarke, T., Kassim, N. Briskin, W. et al. 2016, Society of Photo-Optical Instrumentation Engineers (SPIE) Conference Series, Vol 9906, “Commensal low frequency observing on the NRAO VLA: VLITE status and future plans”, 99065B |
| Blundell, K., Rawlings, S. 2000, AJ, 119, 1111 | |
| Britzen, S., Vermeulen, R. C., Campbell, R. M., et al. 2008, A&A, 484, 119 | |

- Condon J. J., Cotton W. D., Greisen E. W., Yin Q. F., Perley R. A., Taylor G. B., Broderick J. J. 1998, *AJ*, 115, 1693
- Croston J. H., Hardcastle M. J., Harris D. E., Belsole E., Birkinshaw M., Worrall D. M. 2005, *ApJ*, 626, 733
- Croston, J. H., Ineson, J., Hardcastle, M. J., 2018, *MNRAS*, 476, 161
- Davis, S., Laor, A. 2011, *ApJ*, 728, 98
- de Vries, W. H., Barthel, P. D., & O'Dea, C. P. 1997, *A&A*, 321, 105
- Diamond-Stanic, A. M., Fan, X., Brandt, W. N., et al. 2009, *ApJ*, 699, 782
- Douglas, J., Bash, F., Bozyan, F. A., Torrence, G., Wolfe, C. 1996, *AJ*, 111, 1945
- Drinkwater, M., Webster, R., Francis, P. et al. 1997, *MNRAS*, 284, 85
- Dunlop, J. S., Peacock, J. A., Savage, A., Lilly, S. J., Heasley, J. N., Simon, A. J. B 1989, *MNRAS*, 238, 1171
- Evans, I. N., and Koratkar, A. P. 2004, *ApJS*, 150, 73
- Ezeugo, J. and Ubachukwu, A. 2010, *MNRAS*, 408, 2256
- Fanaroff, B. L., Riley, J. M. 1974, *MNRAS*, 167, 31P
- Fender, R., Garrington, S. T., McKay, D. J., et al. 1999, *MNRAS*, 304, 865
- Fey A.L., Charlot P. 2000, *ApJS*, 128, 17
- Fomalont, E. 1999, in *Synthesis Imaging in Radio Astronomy II*, eds. Taylor, G., Carilli, C., Perley, R., ASP Conf. Ser., 180, 301
- Frey S., Gurvits L.I., Kellermann K.I., et al. 1997, *A&A*, 325, 511
- Frey S., Gurvits L. I., Lobanov A. P., Schilizzi R. T., Kawaguchi N., Gabányi K., 2002, in *New Developments in VLBI Science and Technology*, Proc. 6th EVN Symp., eds. Ros, E., Porcas, R. W., Lobanov, A. P., Zensus J. A., Max-Planck-Institut für Radioastronomie, Bonn, p. 89
- Ghisellini, G., Tavecchio, F. and Foschini, L. et al. 2010, *MNRAS*, 402, 497
- Ghisellini, G., Righi, C., Costamante, L., Tavecchio, F. 2017, *MNRAS*, 469, 255
- Ghosh, K. and Punnsly, B. 2007, *ApJL*, 661, 139
- Ginzburg, V. and Syrovatskii, S. 1965, *ARA&A*, 3, 297
- Ginzburg, V. and Syrovatskii, S. 1969, *ARA&A*, 7, 375
- Hardcastle, M., Worrall, D. 2000, *MNRAS*, 314, 359
- Hardcastle, M. J., Harris, D. E., Worrall, D. M., Birkinshaw, M. 2004, *ApJ*, 612, 729
- Hardcastle, M., Evans, D. and Croston, J. 2009, *MNRAS*, 396, 1929
- Homan, D. C., Ojha, R., Wardle, J. F. C., Roberts, D. H., Aller, M. F., Aller, H. D., & Hughes, P. A. 2002, *ApJ*, 568, 99
- Hovatta, T., Valtaoja, E., Tornikoski, M., Lähteenmäki, A. 2009, *A&A*, 498, 723
- Hurley-Walker, N. 2017, arXiv:1703.06635
- Ineson J., Croston J. H., Hardcastle M. J., Mingo B., 2017, *MNRAS*, 467, 1586
- Intema, H. T., Jagannathan, P., Mooley, K. P., & Frail, D. A. 2017, *A&A*, 598, A78
- Kataoka J., Stawarz L. 2005, *ApJ*, 622, 797
- Kellermann, K. I., & Pauliny-Toth, I. I. K. 1969, *ApJ*, 155, L71
- Kellermann, K. I., & Owen, F. 1988, in *Galactic and Extragalactic Radio Astronomy*, eds. Verschuur, G.L., Kellermann, K.I., Springer, p. 577
- Kharb, P., O'Dea, C. Baum, S. et al. 2008, *ApJS*, 174, 74
- Kharb, P., Lister, M. L., Cooper, N. J. 2010, *ApJ*, 710, 764
- Kovalev, Y. Y., Nizhelsky, N. A., Kovalev, Yu. A. et al. 1999, *A&AS*, 139, 545
- Lane, W. M., Cotton, W. D., van Velzen, S., Clarke, T. E., Kassim, N. E., Helmboldt, J. F., Lazio, T. J. W., Cohen, A. S. 2014, *MNRAS*, 440, 327
- Laor, A., Fiore, F., Elvis, M., Wilkes, B., McDowell, J. 1997, *ApJ*, 477, 93
- Lawrence, A., Warren, S., Almaini, O. et al. 2007, *MNRAS*, 379, 1599
- Laor, A., Davis, S. 2014, *ApJ*, 428, 3024
- Lee, S.-S., Lobanov, A., Krichbaum, T. P. et al. 2008, *ApJ*, 136, 59
- Lightman, A., Press, W., Price, R. and Teukolsky, S. 1975, *Problem Book in Relativity and Gravitation*, Princeton University Press, Princeton
- Lind, K., Blandford, R. 1985, *ApJ*, 295, 358
- Li, S., Xia, Z.-Q., Liang, Y.-F., Liao, N.-H., Fan, Y.-Z. 2018, *ApJ*, 853, 159
- Lister, M. L., Cohen, M., Homan, D. et al. 2009, *AJ*, 138, 1874

- Lister, M. L., Aller, M. F., Aller, H. D., et al. 2013, *AJ*, 146, 120
- Lira, P., Kaspi, S., Netzer, H. 2018, *ApJ*, 865, 56
- Marcotulli, L., Paliya, V., Ajello, M. et al. 2020, *ApJ*, 889, 164
- Marziani, P., Sulentic, J., Dultzin-Hacyan, D., Calvani, M., Moles, M. 1996, *ApJS*, 104, 37
- Marziani, P., Sulentic, J., Negrete, A., Dultzin-Hacyan, D., Zamfir, S. et al. 2010, *MNRAS*, 409, 1033
- Marziani, P., Negrete, A., Dultzin, D. et al. 2017, *Front. Astron. Space Sci.*, 4, 16
- Mathews, W. and Brighenti, F. 2003, *ARA&A*, 41 191
- Mattox, J. R., Bertsch, D. L., Chiang, J., et al. 1996, *ApJ*, 461, 396
- Moffet, A. 1975 in *Stars and Stellar Systems, IX: Galaxies and the Universe*, eds. Sandage, A., Sandage, M., & Kristan J., Chicago University Press, Chicago, p. 211
- Murphy, T., Sadler, E., Ekers, R. et al. 2010, *MNRAS*, 402, 2403
- Murray, N., Chiang J. Grossman, S, and Voit, G. 1995, *ApJ*, 451, 498
- Nandra, K., George, I. M., Mushotzky, R. F., Turner, T. J. and Yaquob, T. 1997, *ApJ*, 476, 30
- Neff S.G., Hutchings J.B. 1990, *AJ*, 100, 1441
- Netzer, H., and Marziani, P. 2010, *ApJ*, 724, 318
- O’Dea, C. P., Baum, S. A., & Stanghellini, C. 1991, *ApJ*, 380, 66
- O’Dea, C. 1998, *PASP*, 110, 493
- Orienti, M. and Dallacasa, D. 2008, *A&A*, 487, 885
- Osmer, P.S., Porter, A.C., & Green, R.F. 1994, *ApJ*, 436, 678
- O’Sullivan, S., Gabudza, D., Gurvits, L. 2011, *MNRAS*, 415 3049
- Perley, R. 1982, *AJ*, 87, 859
- Perley, R. and Butler, B. 2013, *ApJS*, 204, 19
- Petrov, L., Gordon, D., Gipson, J., et al. 2009, *J. Geodesy*, 83, 859
- Petrov, L. 2021, *AJ*, 161, 14
- Polisensky, E., Lane, W. M., Hyman, S.D. et al. 2016, *ApJ*, 832, 60
- Punsly, B. 1995, *AJ*, 109, 1555
- Punsly, B. 2008, *Black Hole Gravito-hydro-magnetics*, 2nd ed., Springer-Verlag, New York
- Punsly, B. 2010, *ApJ*, 713, 232
- Punsly, B. 2012, *ApJ*, 746, 91
- Punsly, B., Marziani, P., Zhang, S., Muzahid, S., O’Dea, C. 2016, *ApJ*, 830, 104
- Punsly, B., Tramacere, P., Kharb, P., Marziani, P. 2018, *ApJ*, 869, 164
- Punsly, B. 2019, *ApJL*, 871, L34
- Punsly, B., Hill, G. J., Marziani, P. et al. 2020, *ApJ*, 898, 169
- Pushkarev, A. and Kovalev., Y. 2012, *A&A*, 544, 34
- Rees, M. J. 1966, *Nature*, 211, 468
- Readhead, A. 1994, *ApJ*, 426, 51
- Reed, B. 1989, *Am. J. Phys.*, 57, 642
- Reynolds, C., Punsly, B. Kharb, P., O’Dea, C., and Wrobel, J. 2009, *ApJ*, 706, 851
- Reynolds, C., Punsly, B., Miniutti, G., O’Dea, C., and Hurley-Walker, N. 2020, *ApJ*, 891, 59
- Richards, G., Vanden Berk, D., Reichard, T. et al. 2002, *AJ*, 124, 1
- Sahakyan, N., Israyelyan, D., Harutyunyan, G., Khachatryan, M. and Gasparyan, S. 2020, *MNRAS*, 498, 2594
- Spoelstra, T. A. T., Patnaik, A. R., & Gopal-Krishna 1985, *A&A*, 152, 38
- Steppe, H., Jeyakumar, S., Saikia, D., Salter, C. 1995, *A&AS*, 113, 409
- Sulentic, J., Marziani, P., and Dultzin-Hacyan, D. 2000, *ARA&A*, 38, 521
- Sulentic, J., Bachev, R., Marziani, P., Negrete, C. A., Dultzin, D. 2007, *ApJ*, 666, 757
- Sulentic, J., Martinez-Caraballo, M., Marziani, P. et al. 2015, *MNRAS*, 450, 1916
- Sulentic, J., del Olmo, A., Marziani, P. et al. 2017, *A&A*, 608 122
- Telfer, R., Zheng, W., Kriss, G., Davidsen, A. 2002, *ApJ*, 565, 773
- Tornikoski, M., Jussila, I., Johansson, P., Lainela, M., Valtaoja, E. 2001, *AJ*, 121, 1306
- Tucker, W. 1975, *Radiation Processes in Astrophysics*, MIT Press, Cambridge
- Valtaoja, E., Lähteenmäki, A., Teräsraanta, H., & Lainela, M. 1999, *ApJS*, 120, 95
- van Breugel W. J. M., Fanti C., Fanti R., Stanghellini C., Schilizzi R. T., Spencer R. E. 1992, *A&A*, 256, 56
- van der Laan, H. 1966, *Nature*, 211, 1131
- Wall, J. 1972, *Aust. J. Phys. Suppl.*, 24, 1
- Wayth, R. B., Lenc, E., Bell, M. E. et al. 2015, *PASA*, 32, e025
- Weymann, R.J., Morris, S.L., Foltz, C.B., Hewett, P.C. 1991, *ApJ*, 373, 23

Weymann, R. 1997, in *Mass Ejection from Active Nuclei*, eds. Arav, N., Shlosman, I., and Weymann, R. J., ASP Conf. Ser., 128, 3

Willott, C., Rawlings, S., Blundell, K., Lacy, M. 1999, *MNRAS*, 309, 1017
Wright, E. L. 2006, *PASP*, 118, 1711
Zheng, W., Kriss, G., Telfer, R. et al. 1997, *ApJ*, 475, 469

APPENDIX

A. THE C-BAND DATA IN FIGURES 1 AND 2

Date	Flux Density (mJy)	Telescope	Reference
1968 Aug 03	940 ± 47	Parkes 64m Telescope	Wall (1972)
1980 Nov 18	880 ± 44	VLA	Perley (1982)
1986 Oct 04	940 ± 47	VLA	Drinkwater et al. (1997)
1989 Jan 14	863 ± 86	VLA	This Paper
1989 Mar 30	857 ± 86	VLA	This Paper
1989 May 28	878 ± 88	VLA	This Paper
1989 Dec 08	834 ± 83	VLA	This Paper
1990 Mar 23	854 ± 43	VLA	This Paper
1990 Apr 29	868 ± 43	VLA	This Paper
1990 Jul 08	987 ± 99	VLA	This Paper
1990 Aug 14	917 ± 92	VLA	This Paper
1990 Nov 04	1000 ± 50	VLA	This Paper
1991 Jun 15	905 ± 91	VLA	This Paper
1992 Nov 28	879 ± 88	VLA	This Paper
1993 Jun 12	920 ± 92	VLA	This Paper
1993 Sep 08	920 ± 46	VLA	This Paper
1994 Jan 08	936 ± 47	VLA	This Paper
1995 Sep 13	974 ± 49	VLA	This Paper
1995 Dec 15	954 ± 95	MERLIN	This Paper
1997 Jan 23	924 ± 92	VLA	This Paper
1997 Jun 25	948 ± 95	VLA	This Paper
1997 Jul 20	988 ± 99	VLA	This Paper
1998 Mar 24	914 ± 91	VLA	This Paper
1998 Apr 23	953 ± 53	VLA	This Paper
1998 Jun 02	911 ± 46	VLA	This Paper
1998 Jun 07	919 ± 46	VLA	This Paper
1998 Jun 11	904 ± 45	VLA	This Paper
1998 Aug 20	884 ± 88	VLA	This Paper
1998 Aug 31	883 ± 88	VLA	This Paper
1998 Dec 01	886 ± 44	VLA	This Paper
1998 Dec 05	894 ± 89	VLA	This Paper
2000 Jun 25	844 ± 84	VLA	This Paper
2000 Oct 16	862 ± 43	VLA	This Paper
2002 Mar 11	885 ± 88	VLA	This Paper
2004 Dec 22	902 ± 90	VLA	This Paper
2005 Jun 13	920 ± 46	ATCA	ATCA Calibrator Database
2007 Feb 05	952 ± 49	ATCA	ATCA Calibrator Database
2007 Feb 19	937 ± 47	ATCA	ATCA Calibrator Database
2008 May 28	952 ± 48	ATCA	ATCA Calibrator Database
2009 Feb 15	936 ± 47	ATCA	ATCA Calibrator Database
2010 Feb 13	935 ± 47	ATCA	ATCA Calibrator Database
2011 May 22	988 ± 49	ATCA	ATCA Calibrator Database
2012 Mar 18	959 ± 48	ATCA	ATCA Calibrator Database
2012 Apr 23	960 ± 48	ATCA	ATCA Calibrator Database
2012 Oct 26	945 ± 47	ATCA	ATCA Calibrator Database
2013 Feb 08	946 ± 47	ATCA	ATCA Calibrator Database
2013 May 30	960 ± 48	ATCA	ATCA Calibrator Database
2013 Sep 12	959 ± 48	ATCA	ATCA Calibrator Database
2014 Feb 01	920 ± 46	ATCA	This Paper
2014 Mar 25	946 ± 47	ATCA	ATCA Calibrator Database
2015 Jun 22	888 ± 44	ATCA	This Paper
2015 Jul 11	898 ± 45	ATCA	This Paper
2015 Oct 15	929 ± 46	ATCA	This Paper
2015 Dec 09	912 ± 46	ATCA	This Paper
2016 Jan 13	946 ± 47	ATCA	This Paper
2016 Jan 27	927 ± 46	ATCA	ATCA Calibrator Database
2016 Feb 16	912 ± 46	ATCA	This Paper
2016 Mar 05	894 ± 45	ATCA	This Paper
2016 Apr 14	907 ± 45	ATCA	This Paper
2016 May 08	898 ± 46	ATCA	This Paper
2016 May 18	891 ± 45	ATCA	This Paper
2016 Jun 08	877 ± 44	ATCA	This Paper
2016 Aug 22	868 ± 43	ATCA	This Paper
2016 Sep 29	880 ± 44	ATCA	This Paper
2016 Nov 04	901 ± 45	ATCA	This Paper
2016 Dec 03	886 ± 44	ATCA	This Paper
2016 Dec 05	885 ± 44	ATCA	This Paper
2017 Jan 21	865 ± 43	ATCA	This Paper
2017 Feb 03	862 ± 43	ATCA	This Paper
2017 Mar 02	866 ± 43	ATCA	This Paper
2017 Apr 11	874 ± 44	ATCA	This Paper
2017 Apr 12	873 ± 44	ATCA	ATCA Calibrator Database
2017 May 14	856 ± 43	ATCA	This Paper
2017 Jun 12	876 ± 44	ATCA	ATCA Calibrator Database
2018 Oct 16	858 ± 43	ATCA	ATCA Calibrator Database
2020 Feb 22	843 ± 42	ATCA	ATCA Calibrator Database
2020 Apr 03	858 ± 43	ATCA	ATCA Calibrator Database
2020 Sep 20	836 ± 42	ATCA	ATCA Calibrator Database

B. ERROR ANALYSIS

There are many VLBI observations analyzed Section 3. The observations are quite heterogenous, spanning 33 years. We are unable to access the visibility data for some of the observations reported in the literature. So we cannot estimate uncertainties in the Gaussian component flux density and position using the residuals of the fit to the visibility data, the post-fit rms noise, σ_{rms} (Fomalont 1999; Lee et al. 2008). Our aim is assign uncertainties to the fitted components in a uniform manner. For example, if some references in literature assign liberal uncertainties to component positions and a conservative estimate is implemented on others this will affect the determination of component motion in a weighted least squares fit to the trajectory. So, we are motivated to use an approximate uncertainty in the distance between the nucleus and the components of $\sim 1/5$ of the projection of the elliptical Gaussian synthesized beam FWHM along this direction (Lister et al. 2009, 2013). This can be applied uniformly to all of the observations.

The uncertainty in the component flux densities for the VLBI measurements are of two varieties. Since the core has $> 90\%$ of the total flux, we note that its uncertainty is approximated as the absolute flux density calibration uncertainty of $\approx 10\%$ associated with the VLBI observation (Homan et al. 2002; Pushkarev and Kovalev 2012). This approximation is applied uniformly to all the observations. There is a signal to noise ratio (SNR) driven uncertainty in the total flux density, S , of a component, σ_{tot} , that is the dominant uncertainty for the other much weaker components (Fomalont 1999; Lee et al. 2008). In particular, $\sigma_{\text{tot}} \simeq S(1 + \text{SNR})^{0.5}/\text{SNR}$, where $\text{SNR} = \sigma_{\text{rms}}/S_{\text{peak}}$ and S_{peak} is the peak intensity of the component. But as stated above, σ_{rms} is not known or derivable in some cases. In order to derive a uniform estimate of the uncertainty of the flux density, we computed the SNR driven uncertainty for numerous cases for which we could determine σ_{rms} . This uncertainty was added in quadrature with the 10% absolute calibration uncertainty. There are three components (besides the core) that appear in our fits in Tables 1, 3 and 4. For various observations, we estimate a total uncertainty of $\sim 40\%$ in the North Lobe flux density, $S_{\text{North Lobe}}$, $\sigma_{\text{North Lobe}} \approx 0.4S_{\text{North Lobe}}$. The other components are nearly point sources (S measured in mJy $\approx S_{\text{peak}}$ measured in mJy beam $^{-1}$) and theoretically the uncertainty should scale approximately with flux density, S , as $(\sigma_{\text{component}}/S) \approx 0.4(S_{\text{North Lobe}}/S)^{0.5}$. Our uncertainty estimates verify this to be true empirically as well. Using this prescription, we can uniformly apply these approximate uncertainties to all the Gaussian brightness distribution models in this paper. None of our results in Section 8 depend strongly on the precise magnitudes of these uncertainties in flux density.